Chapter 6

Sub-granular Scale Misorientation and Strain Accommodation

In the previous chapters, microstructural evolution and constitutive response was examined with varying temperature, strain rate, and strain during high temperature compression of René 88DT. Dominant deformation mechanisms vary with temperature (T) and strain rate ($\dot{\varepsilon}$) over the range of T = 1241K (968˚C) to 1323K (1050˚C) and $\dot{\varepsilon}$ = 0.00032/s to 0.1/s. Power-law creep deformation occurs during low temperature and high strain rate deformation, where as superplastic deformation is more favorable at high temperatures and low strain rates. Additionally, dynamic recrystallization is observed at high strain rates where power-law creep deformation is favorable. To build models for structure evolution, it is necessary to examine how strain accumulates at the grain scale during deformation at different temperatures and strain rates and also how strain is retained post-deformation. Until the development of the EBSD technique, there was no efficient way of analyzing strain accumulation over large volumes of material at high resolution. Transmission electron microscopy (TEM) was used to analyze dislocation structure, but TEM samples are very thin, making analyzing areas larger than $50\mu m^3$ difficult. In this chapter, EBSD misorientation data is used to analyze strain accumulation and storage

during high temperature deformation of René 88DT at a higher resolution than strain mapping, which was discussed in Chapter 3.

6.1 Experimental Procedure

Orientation data collected via EBSD scans has been used to calculate local misorientation at the scale of individual grains. EBSD experimental data presented in this chapter was all collected with a scan step size of 0.2μm. Using a SEM accelerating voltage of 20kV, the beam sampling depth for Ni is ~40nm. The collected EBSD data undergoes the same cleaning algorithm as grain size data. However, twin boundaries are identified as grain boundaries when calculating misorientation so that twin offsets are not counted into transgranular misorientation. Local misorientation within grains can be characterized in several different ways:

1. Kernel Average Misorientation (KAM)
2. Grain Average Misorientation (GAM)
3. Grain Reference Orientation Deviation (GROD)
4. Grain Orientation Spread (GOS)

KAM is the average misorientation of a scan point from all closest neighboring points. EBSD scans sample orientation in an octahedral pattern, which means that each scan point has 6 nearest neighbor points. Therefore, KAM is the average misorientation of a scan point from all 6 of its nearest neighbor points. KAM is the best measurement of local misorientation; furthermore, it is the only misorientation measurement with a defined area of measurement. KAM has been proven to be qualitatively representative of dislocation density within regions of grains [65]. The average of KAM over each grain is the grain average misorientation (GAM). GROD

is measured by calculating the orientation difference between each scan point within a grain to the average orientation of the grain. GROD maps are useful in visually understanding the lattice strain across the grain but are not useful as a quantitative data across a range of grain sizes because large grains with large lattice strain across the grain skew the average GROD to higher values. GOS is a measurement corresponding to the average GROD of each point within a given grain meaning that every grain gets a single average GROD value, therefore eliminating grain size effects.

6.2 Temperature and Strain Rate Varying Misorientation Evolution

Two sets of experiments were conducted on René 88DT to determine misorientation and evolution of strain distribution at the grain scale during high temperature compression. The first set of experiments was conducted to determine the temperature and strain rate effects of misorientation and strain accumulation. Test temperatures ranged from 1241K (968˚C) to 1323K (1050˚C) and the tested strain rates range from 0.00032/s to 0.1/s. A true strain of 110% was imposed on all samples.

6.2.1 Experimental Results

6.2.1.1 Measured Misorientation

Figure 6.1 shows a map of GROD plots for the set of experiments on compression samples where each column represents a different strain rate and each row represents a different temperature. All scans are 40x40μm and the colors represent different bins of calculated orientation deviation as described by the scale

bar on the right side. The as-extruded GROD map is also illustrated on the right hand side for comparison. The scans show that a small fraction of the grains in the as-extruded microstructure contain high degrees of misorientation. This misorientation is a result of the strain imposed during the extrusion process. A fraction of this misorientation is recovered during the heating of the samples to temperature; the average GOS of the as-extruded material is 0.46˚ while the average GOS of samples after heating to test temperatures but before deformation are between 0.39˚ and 0.41˚. As shown in Figure 6.1, during compression, the frequency of grains with >0.7˚ orientation deviation increases as both strain rate and temperature increase, indicating that more misorientation is accumulating transgranularly despite the same imposed strain on all samples. The average GOS as a function of strain rate for samples compressed at each test temperature is shown in Figure 6.2. In addition to the increase in misorientation with increasing strain rate, as observed by the GROD maps, the GOS plateaus between 0.032/s and 0.1/s strain rate for all temperatures.

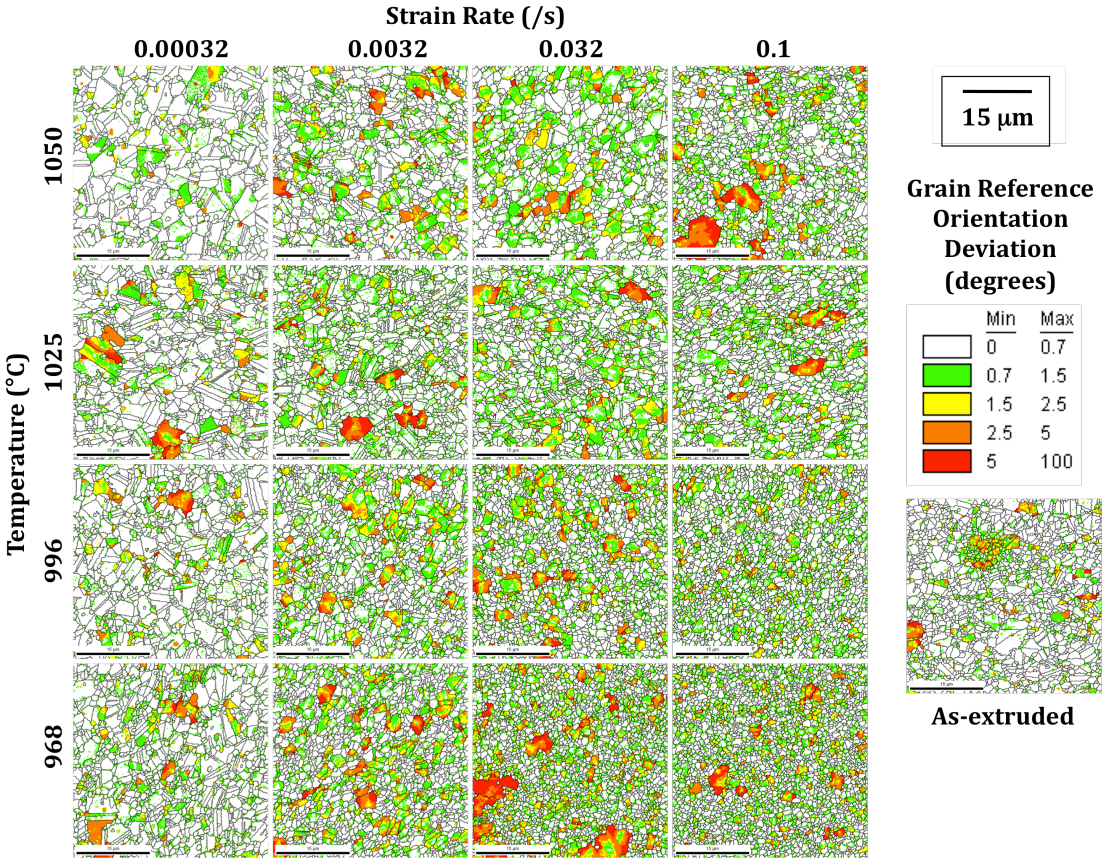

Figure 6.1: GROD Map of René 88DT compressed at different temperature and strain rate. As-extruded GROD is shown on the right along with GROD scale.

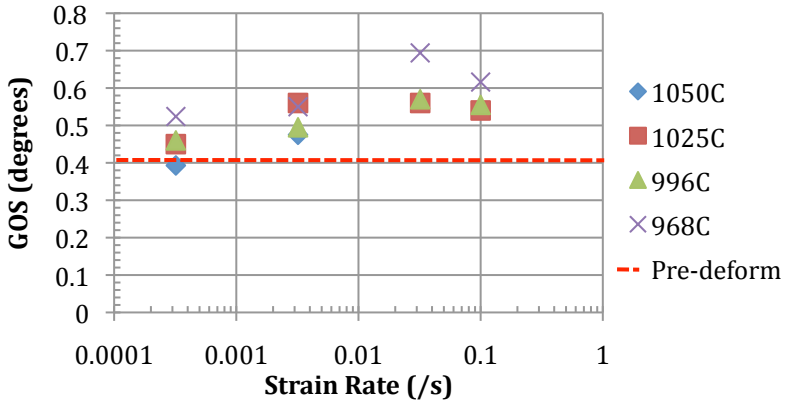

Figure 6.2: Average grain orientation spread as a function of strain rate for René 88DT compressed at different temperatures. Red line shows average pre-deformation GOS.

Figure 6.3 plots the KAM maps as a function of strain rate and temperature. The maximum KAM measured at all test conditions with an EBSD scan step size of 0.2µm was 3°. In grains with high average KAM, the misorientation is not distributed evenly; bands of high KAM across grains are commonly observed. Figure 6.4 shows

examples of high KAM bands (orange and green lines) across grains after compression.

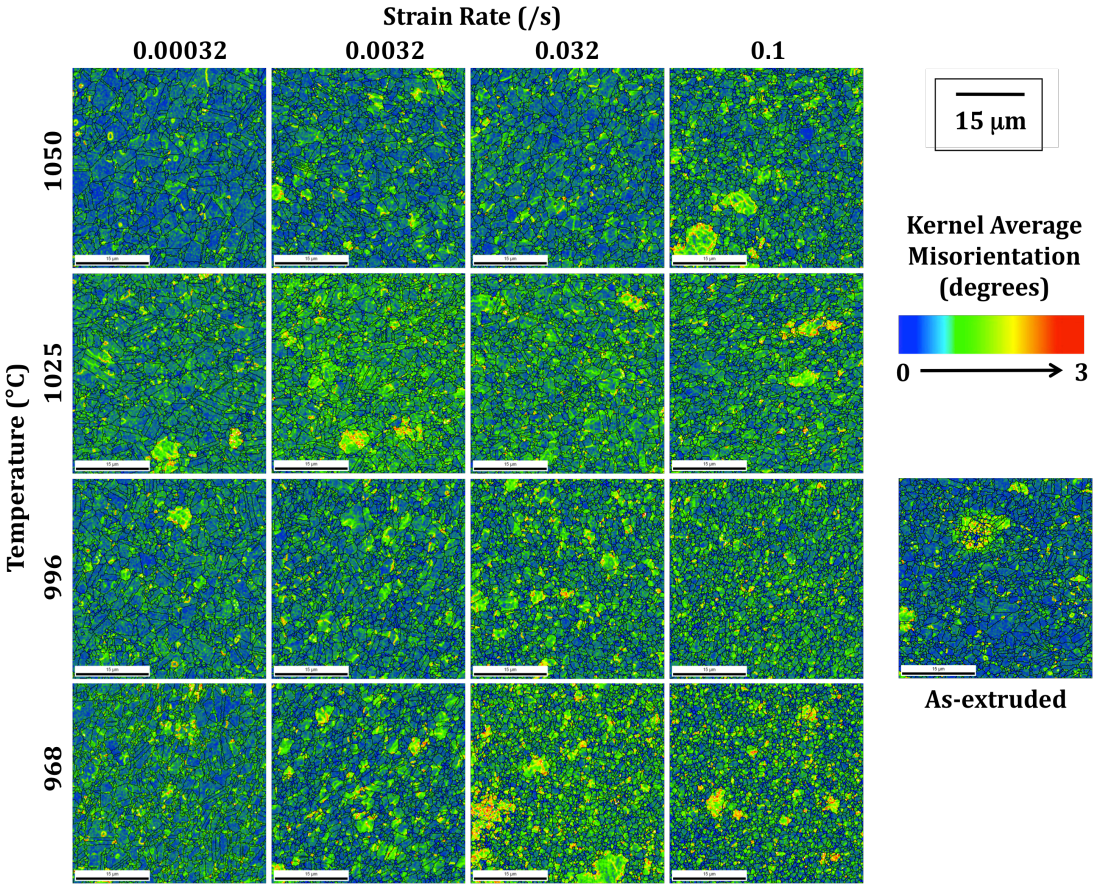

Figure 6.3: KAM Map of René 88DT compressed at different temperature and strain rate. As-extruded KAM is shown on the right along with scale.

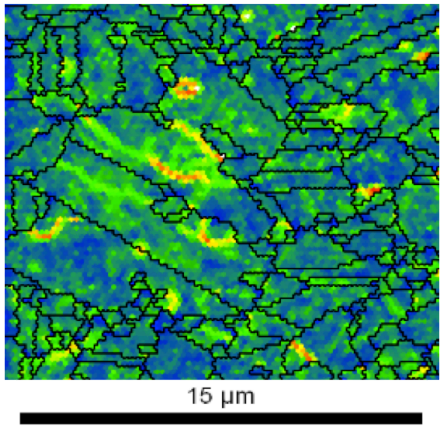

Figure 6.4: Local KAM region showing misorientation substructure within grains as indicated by bands of high KAM in green and red.

Average KAM and GAM are shown in Figures 6.5 and 6.6 respectively. During deformation at 1323˚K (1050˚C) using low strain rates, misorientation decreases when compared to the as-extruded misorientation. At higher strain rates and lower temperatures, the measured KAM and GAM increases when compared to the as-extruded levels. In general, both KAM and GAM increase with decreasing temperature.

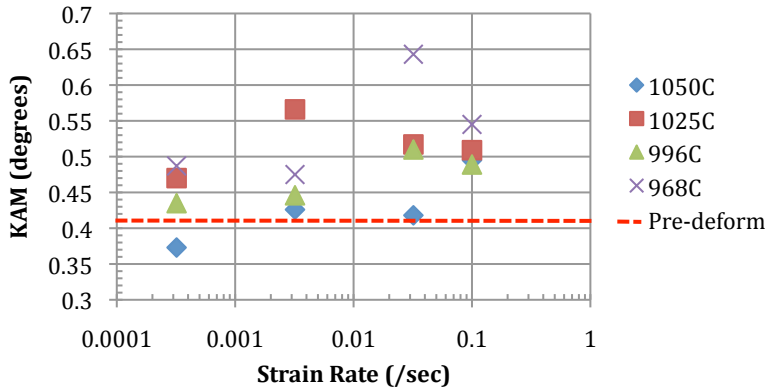

Figure 6.5: Average KAM as a function of strain rate for René 88DT compressed at different temperatures.

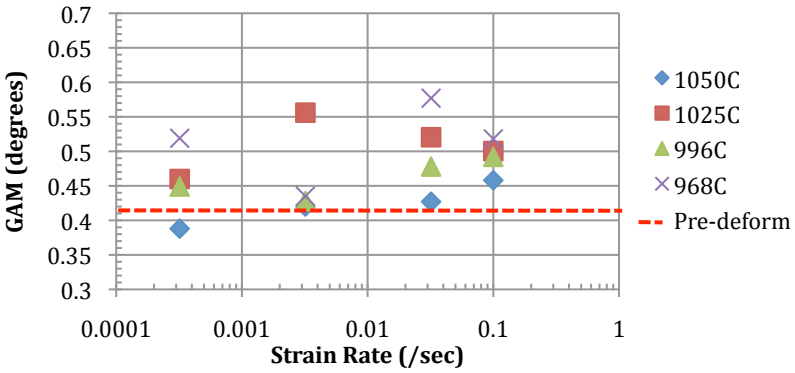

Figure 6.6: GAM as a function of strain rate for René 88DT compressed at different temperatures.

6.2.1.2 GAM Distributions

Figures 6.7 – 6.10 shows the GAM distributions as a function of strain rate for each test temperature. The GAM distribution width increases as strain rate increases at all test temperatures. To model the evolution of GAM with temperature, strain rate, and strain, the GAM distributions need to be fit to mathematical distributions and the

evolution of the distribution parameters evaluated. The GAM distributions fit Log-Lorentzian distributions with the form:

$$L(x) = \frac{A}{1 + \left(\frac{\log(x) - \log(x_0)}{s} \right)^2} \qquad [6\text{-}1]$$

where x is GAM, A is the amplitude, x_0 is the location parameter, and s is the standard deviation. Figure 6.11 compares the experimental GAM distribution of René 88DT sample compressed at 1241˚K (968˚C) using 0.032/s strain rate to the Log-Lorentzian distribution fit.

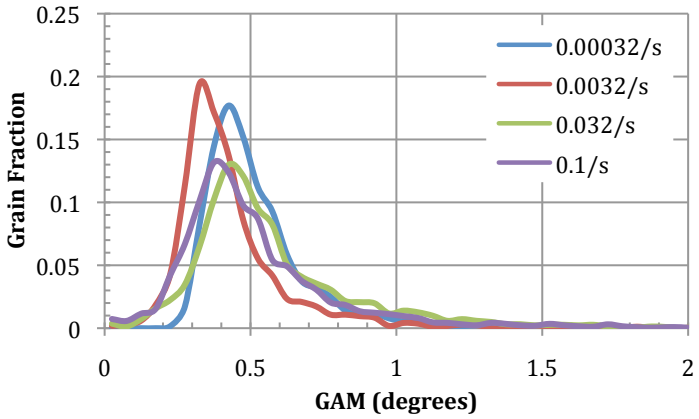

Figure 6.7: GAM distribution for René 88DT compressed at 1241˚K (968˚C).

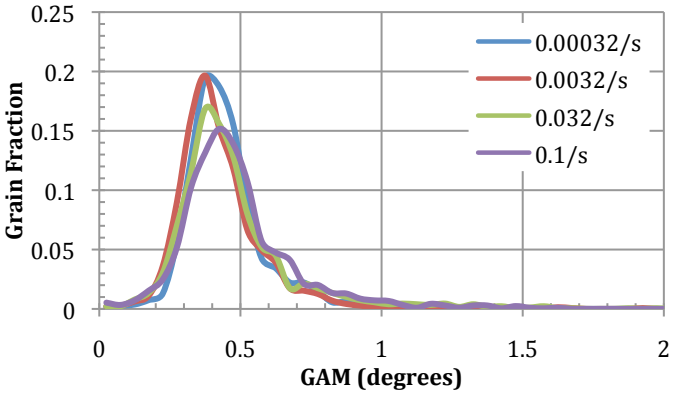

Figure 6.8: GAM distribution for René 88DT compressed at 1269˚K (996˚C).

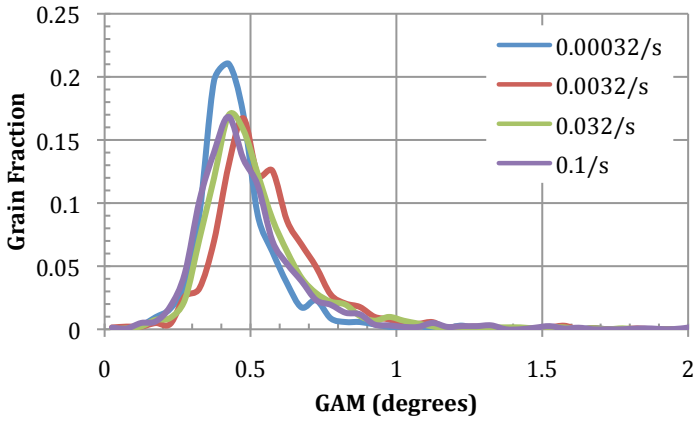

Figure 6.9: GAM distribution for René 88DT compressed at 1298˚K (1025˚C).

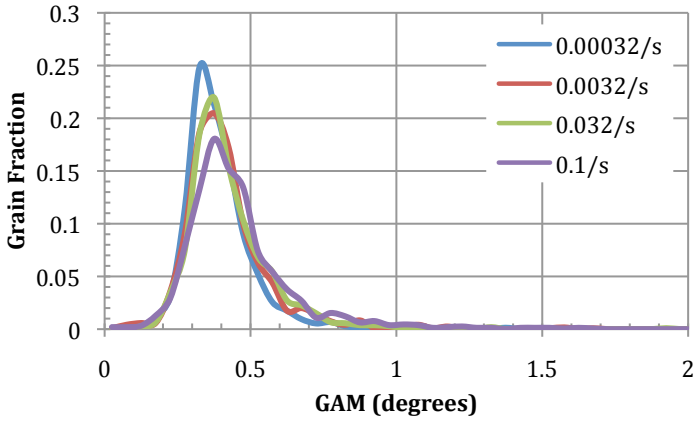

Figure 6.10: GAM distribution for René 88DT compressed at 1323˚K (1050˚C).

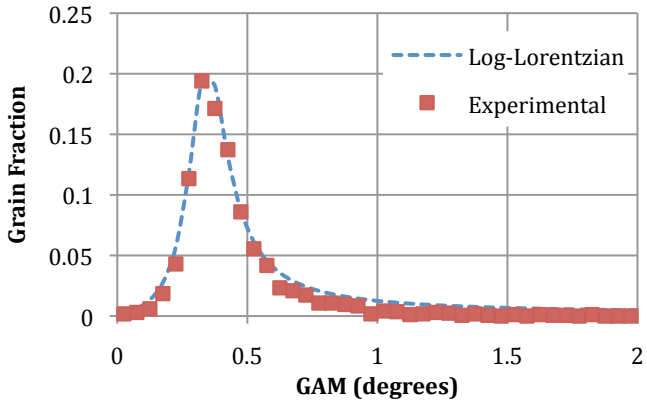

Figure 6.11: Experimental GAM distribution of René 88DT compressed at 1241K (968˚C) using 0.032/s strain rate compared to the Log-Lorentzian distribution fit.

The standard deviation (*s*), a measure of the width of the distribution, is plotted as a function of strain rate for all test temperatures in Figure 6.12. The figure shows that the standard deviation increases as strain rate increases and temperature decreases.

Increase in the standard deviation increases the width of the fit on the GAM distribution meaning that the GAM distribution broadens as strain rate increases and temperature decreases. Furthermore, as the GAM distribution broadens, the height of the peak decreases, as illustrated by the amplitude (A) of the Log-Lorentzian distribution fit as a function of strain rate shown in Figure 6.13. Despite the change in shape of the distribution, the position of the Log-Lorentzian distribution fit stays relatively constant, as shown by Figure 6.14, which plots the distribution peak position (x_0) as a function of strain rate.

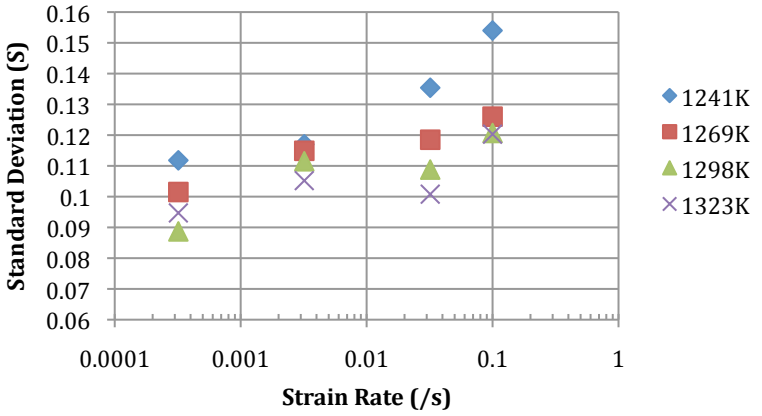

Figure 6.12: Log-Lorentzian distribution standard deviation for GAM distribution fits as a function of strain rate for various temperatures.

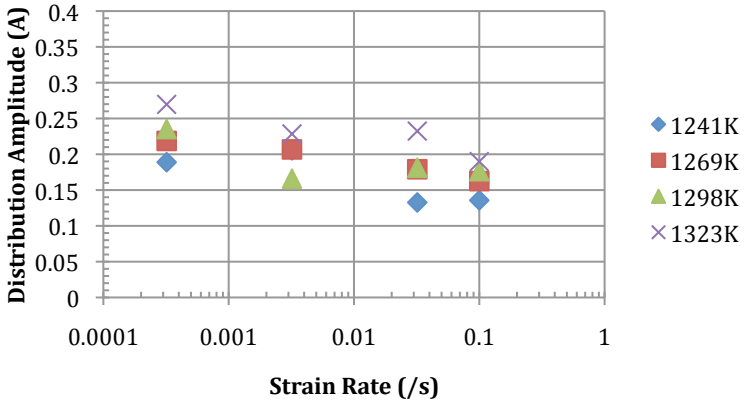

Figure 6.13: Log-Lorentzian distribution amplitude (A) for GAM distribution fits as a function of strain rate for various temperatures.

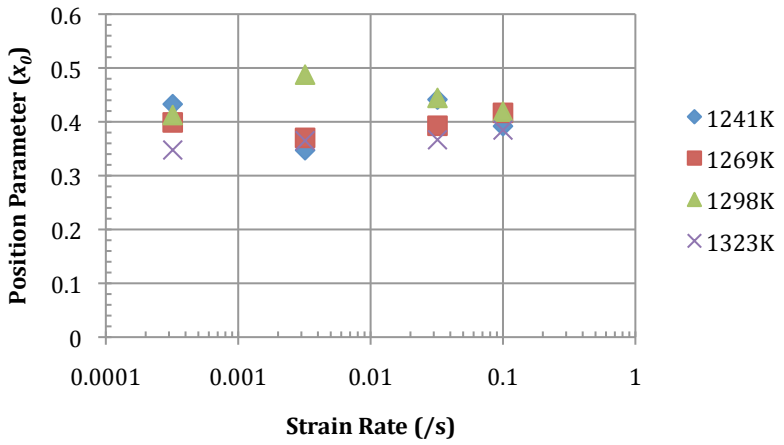

Figure 6.14: Log-Lorentzian distribution peak position (x_0) for GAM distribution fits as a function of strain rate for various temperatures.

The evolution of the three measured parameters into the Log-Lorentzian distribution quantifies the evolution of GAM as a function of temperature and strain rate, which is useful in modeling the evolution of strain storage during deformation of René 88DT.

6.2.1.3 Grain Size Dependence of Average Misorientation

To analyze the grain size dependence of misorientation accumulation during high temperature deformation of René 88DT, all grains within each scan were separated into bins according to the grain size. It is important to note that the grain sizes are artificially smaller than the true grain sizes because all twin boundaries are considered grain boundaries to discard misorientation across twin boundaries. If it is assumed that half of the grains have one twin boundary, then the average grain size of the sample would be 0.75 of the true size. Each identified grain has an associated GAM, which is averaged for grains in each bin. The grains were separated into diameter (D) bins in 0.5μm intervals up to 5μm. All grains larger than 5μm in diameter were counted into the last bin. Figure 6.15 shows the average GAM as a

function of grain size for the as-extruded material. The measured GAM stays relatively constant as a function of grain size. There is even a slight decrease in the average GAM in the largest grains.

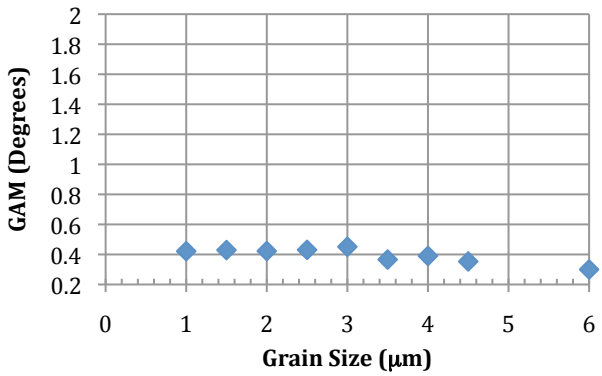

Figure 6.15: Average GAM as a function of grain size for the as-extruded René 88DT material.

Figures 6.16 – 6.19 show average GAM as a function of grain size for samples deformed at different strain rates at each test temperature. The average GAM for grains below 2μm is generally between 0.4˚ and 0.6˚ for all 4 strain rates at 1241K (968˚C). But as strain rate increases from 0.00032/s to 0.1/s, the accumulated GAM measured in the larger grains increases as strain rate increases. This phenomenon of increased accumulated GAM with increasing grain size is observed at all temperatures, but the magnitude of the increase decreases as temperature increases; the observed increase in GAM as a function of strain rate within the larger grains is much less for samples compressed at 1323K (1050˚C) when compared to those compressed at 1241K (968˚C).

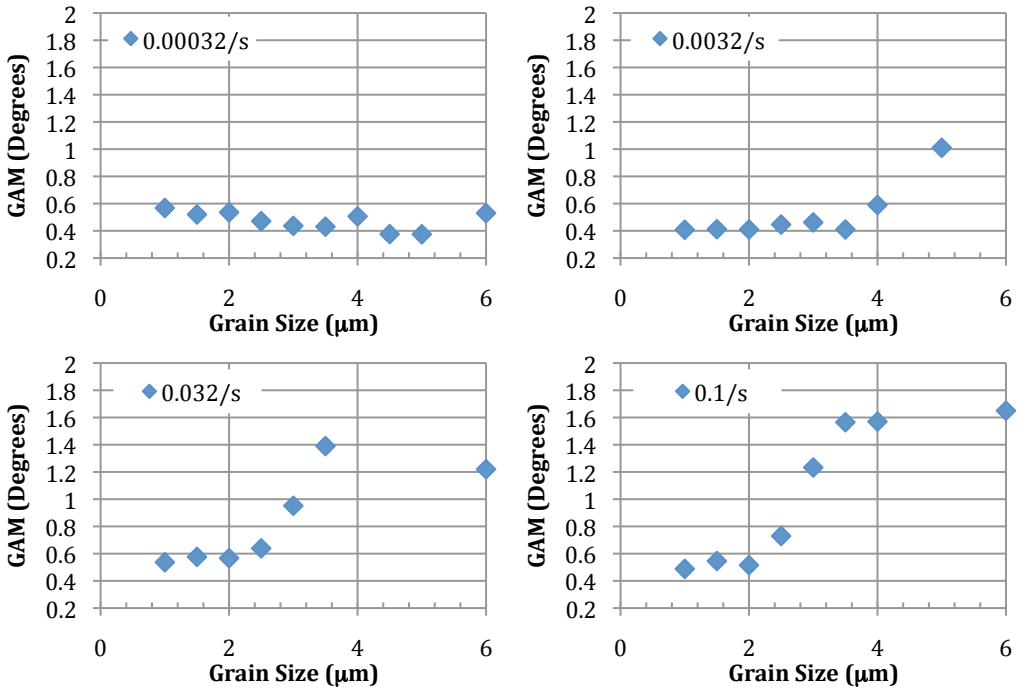

Figure 6.16: Plots of GAM as a function of grain size for René 88DT samples compressed at 4 different strain rates, all at 1241K (968˚C).

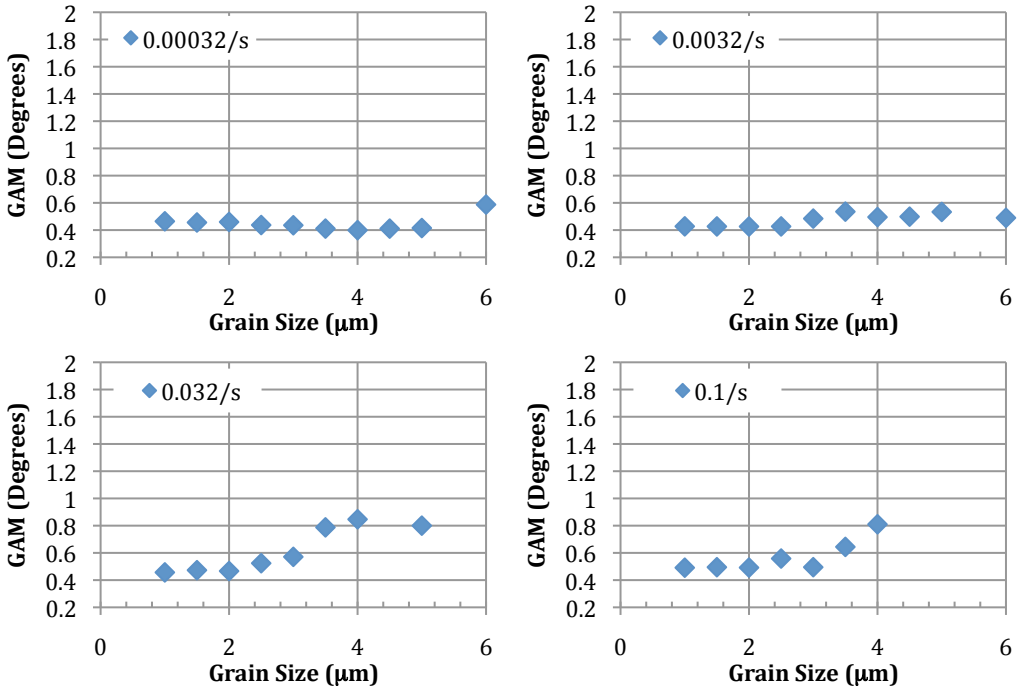

Figure 6.17: Plots of GAM as a function of grain size for René 88DT samples compressed at 4 different strain rates, all at 1269K (996˚C).

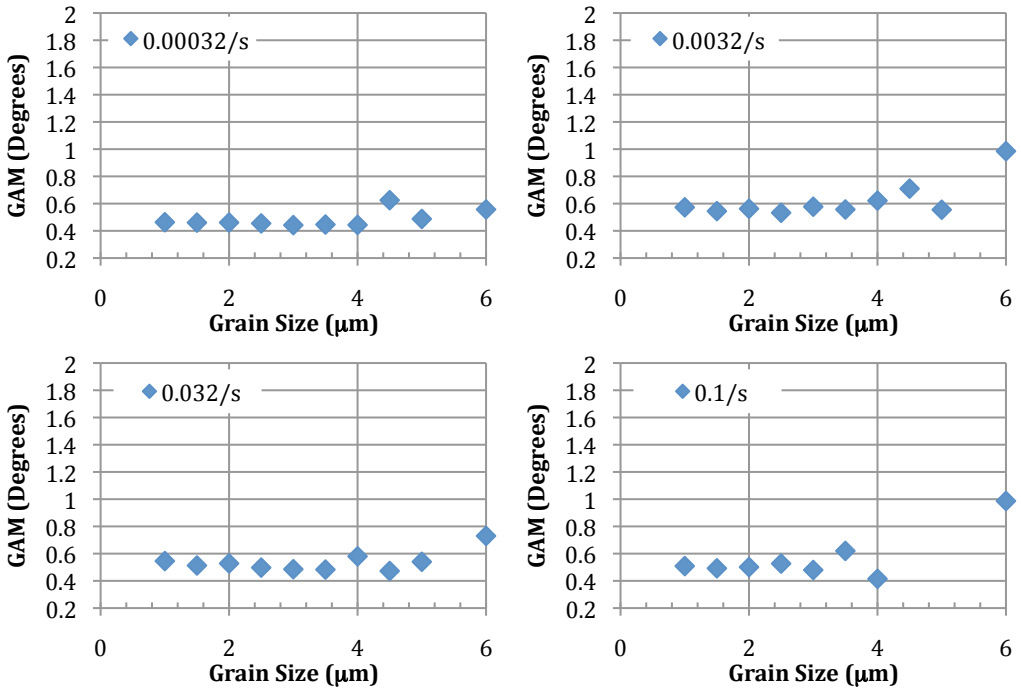

Figure 6.18: Plots of GAM as a function of grain size for René 88DT samples compressed at 4 different strain rates, all at 1298K (1025˚C).

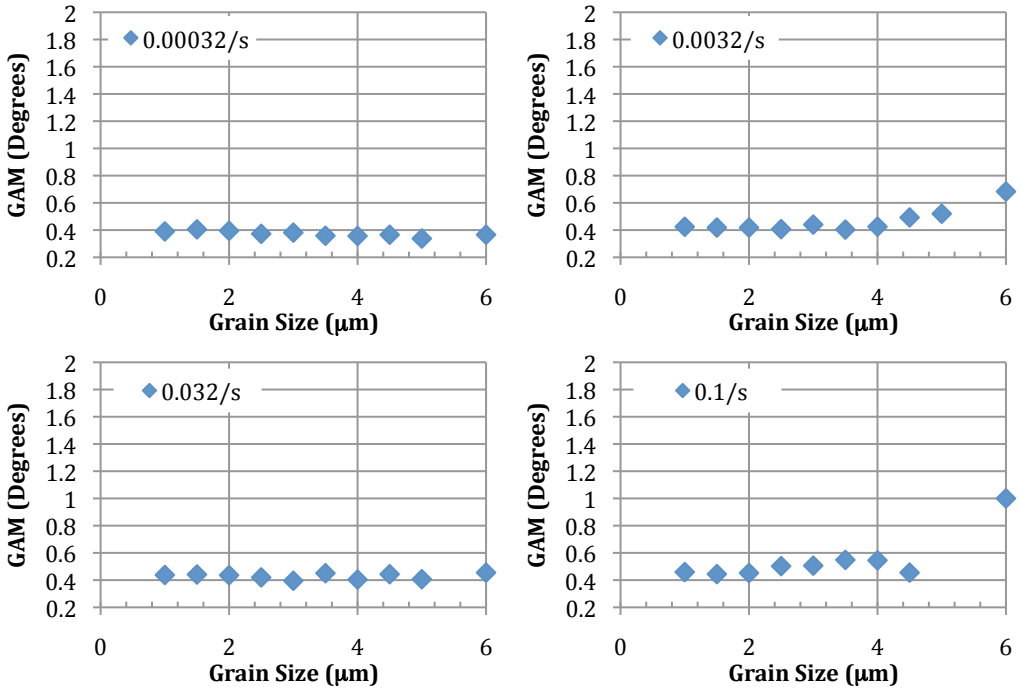

Figure 6.19: Plots of GAM as a function of grain size for René 88DT samples compressed at 4 different strain rates, all at 1323K (1050˚C).

6.2.1.4 Taylor Factor

Due to the inhomogeneity of the misorientation accumulation during compression, Taylor factors were calculated for all EBSD sample scans to determine relationship between grain orientation and misorientation retained. Figure 6.20 shows GROD and Taylor factor maps for 2 samples compressed at different strain rates and at different temperatures. The average Taylor factor for all test samples ranged from 3.03 – 3.08, which matches the FCC crystal structure Taylor factor with [1 1 1]<110> slip systems. The spread of the Taylor factor for individual grains ranges from 2.2 to 3.7, but there is no correlation between measured Taylor factor and average grain misorientation.

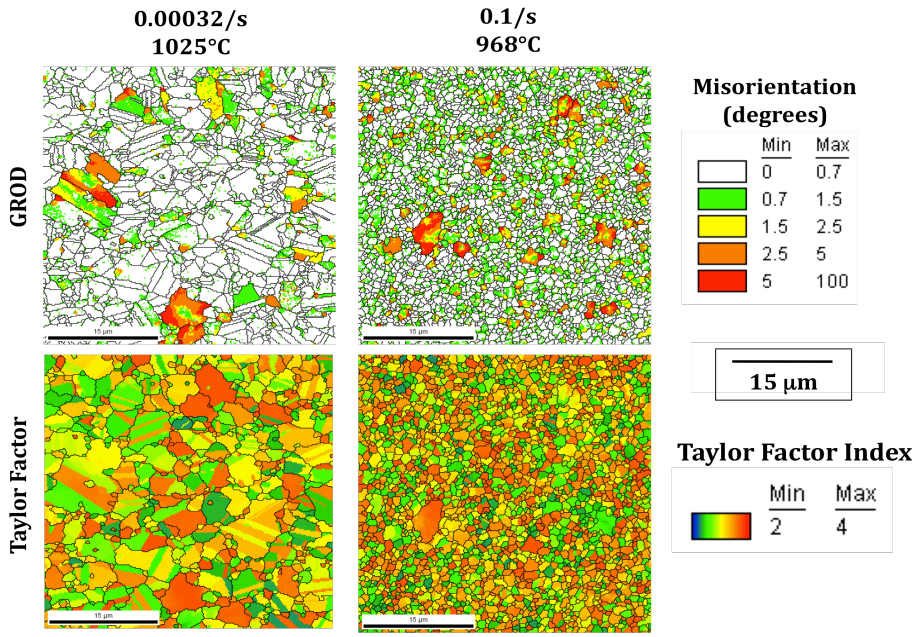

Figure 6.20: GROD and Taylor factor maps for samples compressed at 2 different strain rates and temperatures as labeled on top of each map.

6.2.2 Discussion

Experimental evaluations of the evolution of flow stress as a function of strain rate, discussed in Chapter 4, indicates that as-extruded René 88DT deforms

predominately by superplastic deformation at strain rates below 0.0032/s at test temperatures. At those temperatures, grain coarsening occurs as γ' undergoes rapid dissolution during deformation, as discussed in chapter 5. EBSD misorientation results shown in this chapter indicate that during superplastic deformation, very little misorientation accumulates within grains; GROD maps show very limited lattice strain across grains and average GOS, KAM, and GAM for samples deformed at the lowest strain rate are comparable to the as-extruded levels. These low levels of measured misorientation suggest that majority of strain is accommodated by grain boundary sliding, the primary mechanism for superplastic deformation. However, as strain rate increases at all test temperatures, misorientation collected within grains during compression increases. GROD maps and GOS distributions show that distribution of misorientation accumulated during deformation is not homogeneous; some grains retain substantial amount of misorientation while others collect very little, as shown by the broadening of the GAM distribution. Nevertheless, average GOS, KAM, and GAM all increase with increasing strain rate. This increase in strain storage within grains indicates that strain accommodation by grain boundary sliding becomes less favorable as temperature decreases from 1323K (1050˚C) to 1241K (968˚C). Therefore, the transition between superplastic deformation to power-law creep deformation occurs at slower strain rates as deformation temperature decreases.

Analysis of the grain size dependence of misorientation accumulation showed that larger grains (D > 2μm) accumulate more misorientation at both high strain rates and also low temperatures, while accumulation of misorientation becomes less grain size dependent as temperature and strain rate decreases. The strain rates at which

misorientation becomes grain size dependent are those strain rates where power-law creep deformation is observed. The larger grains accumulate more strain transgranularly during deformation under power-law creep conditions. This phenomenon can be explained by the grain size dependence of superplasticity. It is well known that during superplastic deformation, grain boundary sliding and grain rotation are more favorable for smaller grains. Therefore, grain boundary sliding and grain rotation are more likely for smaller grains, suggesting that a portion of the imposed strain can be accommodated by those deformation mechanisms. Grain boundary sliding and grain rotation is less favorable for large grains, therefore the majority of the imposed strain will be accommodated transgranularly in the larger grains, which means more misorientation is expected in larger grains at strain rates near the superplastic to power-law transition. Evidence of grain size dependent strain accumulation is also important for dynamic recrystallization; higher stored strain within larger grains means that initiation of nucleation will most likely occur within or at the grain boundaries of the larger grains.

As compression strain rate increases for a constant test temperature, misorientation accumulation within grains also increase. But as average GOS, GAM, and KAM show, misorientation does not increase linearly with strain rate. Misorientation increases between 0.0032/s and 0.032/s strain rates and plateaus at a higher strain rate. To examine the transition from low to high retained misorientation, compression tests on additional samples at strain rates between 0.001/s and 0.01/s were conducted for a constant temperature. The next section of this chapter discusses

misorientation accumulation during deformation of René 88DT at 1298K (1025˚C) for varying strain rates.

6.3 Strain Rate Dependence of Misorientation Accumulation at 1298K (1025˚C)

6.3.1 Experimental Results

6.3.1.1 Average Misorientation Accumulation

To analyze the evolution of accumulated misorientation as a function of strain rate for René 88DT compressed at 1298K (1025˚C), 15 samples were compressed at 15 different strain rates, all with imposed true strain of 110%. The strain rates ranged from 0.00032/s to 0.1/s. Figure 6.21 shows the average GOS of all 15 samples as a function of strain rate. It is apparent that the average GOS stays at 0.45˚ until a strain rate of 0.001/s, at which point subsequent increases in strain rate result in an increase in average GOS. Once a strain rate of 0.0032/s is reached, the average GOS plateaus, though there is a high degree of variance in average GOS for higher strain rates.

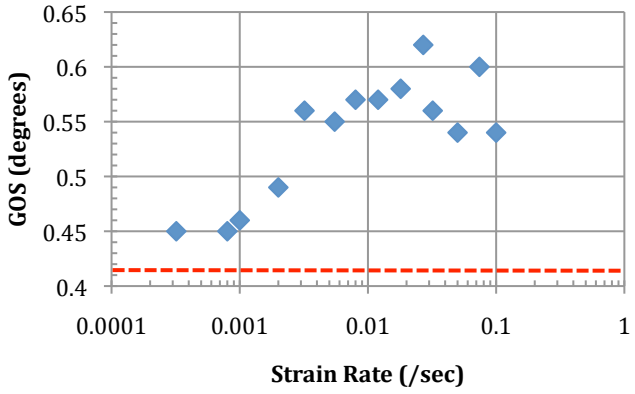

Figure 6.21: Grain orientation spread (GOS) of René 88DT samples compressed at various strain rates at 1298K (1025˚C). Red line indicates the pre-deformation level.

Figures 6.22 and 6.23 show average KAM and GAM respectively. Each shows an increase in respective misorientation between 0.001/s and 0.01/s strain rates. The

misorientation stays relatively constant for strain rates slower and faster to the two respectively. The plateau in both KAM and GAM at high strain rate occurs between 0.5˚ and 0.55˚.

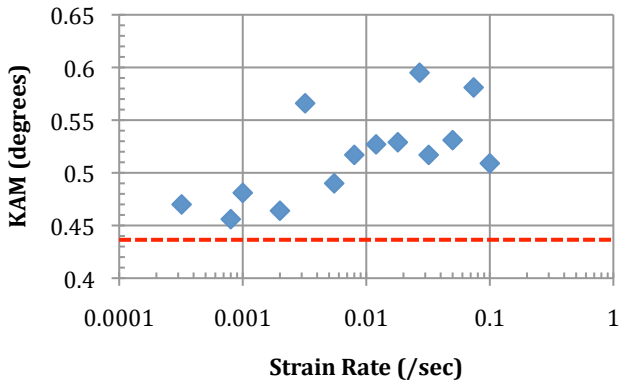

Figure 6.22: Average KAM for René 88DT compressed at various strain rates at 1298K (1025˚C). Red line indicates the pre-deformation level.

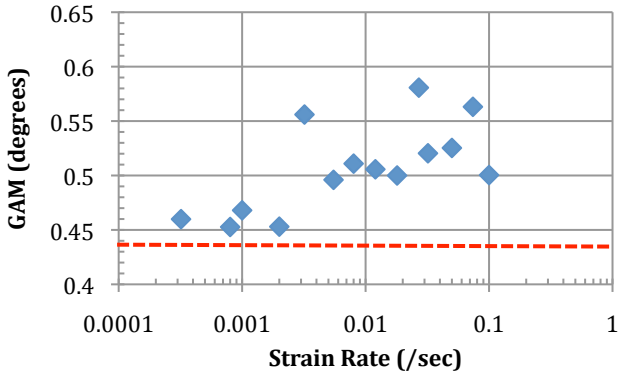

Figure 6.23: Average GAM for René 88DT compressed at various strain rates at 1298K (1025˚C). Red line indicates the pre-deformation level.

6.3.1.2 GAM Distribution Analysis

As expected the standard deviation (S) of the Log-Lorentzian fit of the GAM distribution shows a broadening of GAM as strain rate increases (Figure 6.24). The amplitude (A) of the Log-Lorentzian fit is inversely proportional to the standard deviation, decreasing as the GAM distribution broadens, as shown in Figure 6.25. The distribution peak position (x_0) follows an exponential curve, which increases at high

strain rates. Figure 6.26 shows that x_0 (μm) as a function of strain rate can be described by:

$$x_0 = 0.4207\exp(2.491\dot{\varepsilon}) \qquad [6\text{-}1]$$

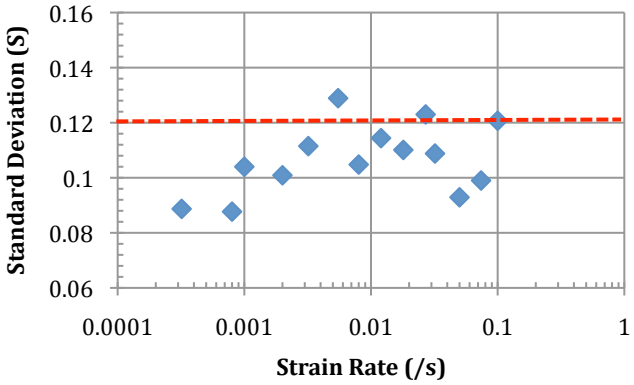

Figure 6.24: Standard deviation (S) of Log-Lorentzian fit of GAM distribution for samples compressed at 1298K (1025˚C). Red line indicates the pre-deformation level.

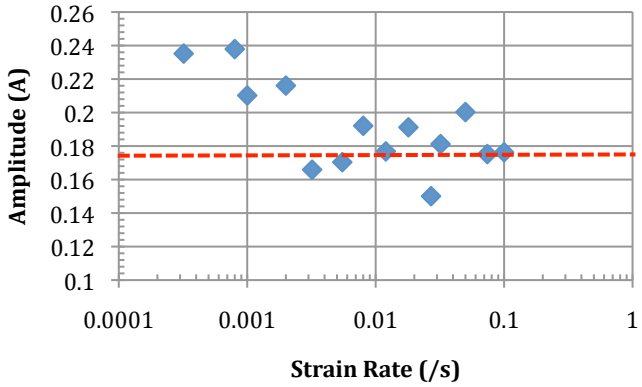

Figure 6.25: Amplitude (A) of Log-Lorentzian fit of GAM distribution for samples compressed at 1298K (1025˚C). Red line indicates the pre-deformation level.

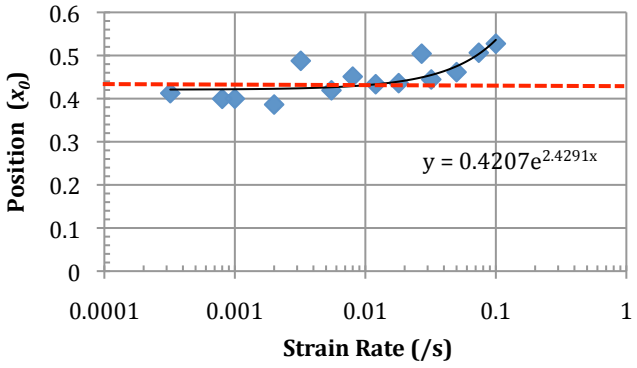

Figure 6.26: Position parameter (x_0) of Log-Lorentzian fit of GAM distribution for samples compressed at 1298K (1025˚C). Red line indicates the pre-deformation level.

6.3.2 Discussion

The misorientation collected at strain rates lower than 0.001/s is stable at an average GOS of 0.45, and an average KAM and GAM of 0.47˚. Very little misorientation collects compared to the as-extruded sample, which had a measured GOS of 0.43˚, and an average KAM and GAM of 0.44˚. Samples compressed at the strain rates below 0.001/s are expected to deform superplastically, with dissolution of γ', which causes grain growth, which subsequently promotes strain hardening. Therefore, it can be concluded that during superplastic deformation, very little transgranular misorientation accumulates.

Misorientation collected during deformation at strain rates above 0.01/s plateaus at a GOS between 0.55˚ and 0.6˚, and a KAM and GAM between 0.5˚ and 0.54˚. Large misorientation measured in a few samples above these ranges have relatively low EBSD scan confidence index and therefore are not considered accurate. Nevertheless, the average misorientation measured is much higher than both the pre-deformation and slow strain rate deformation levels. Furthermore, deformation at these strain rates occurs by power-law creep, as indicated by a strain rate sensitivity coefficient below 0.2, as shown in chapter 4. Therefore, EBSD misorientation data indicates that high degrees of misorientation accumulate transgranularly during power-law creep deformation.

EBSD misorientation data shows that misorientation collected scales with strain rate during compression at intermediate strain rates between 0.001/s and 0.01/s. At these strain rates, the strain rate sensitivity is transitioning from above 0.4 to below 0.2, indicating that the deformation mechanism is transitioning from superplastic to

power-law creep. The misorientation data also indicate that transgranular deformation also increases during compression at intermediate strain rates. As strain rate increases, the size of grains that can accommodate grain boundary sliding necessary for superplastic deformation decreases causing larger grains to deform by power-law creep. Therefore, deformation mechanisms during compression at these intermediate strain rates depends on local grain structure, which varies with average grain size. A model predicting deformation mechanisms during high temperature compression will be discussed in the next chapter.

6.4 Strain Dependent Misorientation Evolution

It has been shown in the previous sections of this chapter that accumulated transgranular misorientation evolves with strain rate. At high strain rates where power-law creep deformation mechanisms dominate, high degrees of misorientation collect within grains. At low strain rates where superplastic deformation mechanisms dominate, very little misorientation collects within grains. But the evolution of accumulated misorientation as a function of strain is still not well understood for different deformation mechanisms. EBSD misorientation data for René 88DT compressed to varying strain increments for varying strain rates will be presented in the next section, followed by a discussion of observed results.

6.4.1 Experimental Results

To analyze progression of misorientation accumulation with strain, René 88DT samples were compressed at 0.001/s, 0.0055/s, 0.018/s, and 0.05/s strain rates in increments of 0.1 engineering strain up to 0.5. Average GOS, KAM, and GAM were measured for each sample along with the grain size distributions. Figures 6.27 –

6.29 show the progression of average GOS, KAM, and GAM for each strain rate respectively. The figures show that at 0.001/s strain rate, there is minimal accumulation of misorientation. At 0.0055/s strain rate, there is an initial accumulation of misorientation at engineering strain (**e**) = 0.1, followed by consistent recovery of the misorientation. At 0.018/s strain rate, the misorientation collected oscillates as a function of strain. At the highest strain rate of 0.05/s, the misorientation increases gradually as a function of strain.

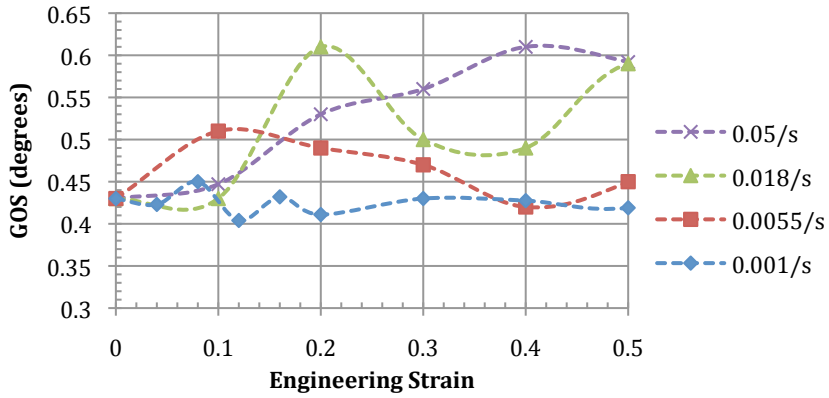

Figure 6.27: Average GOS of René 88DT samples compressed at different strain rates in 0.1 strain increments.

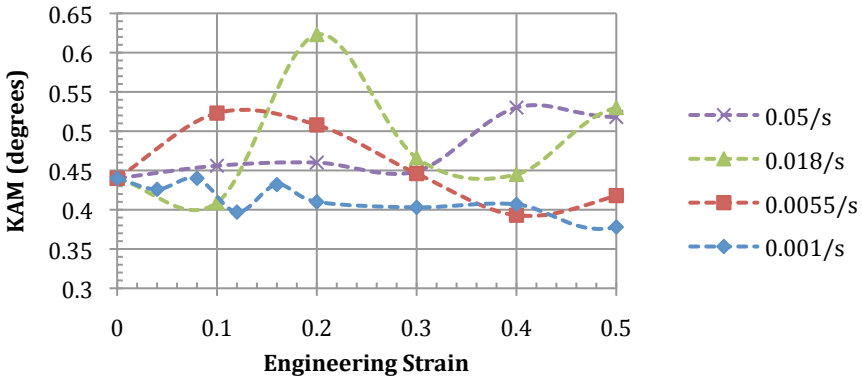

Figure 6.28: Average KAM of René 88DT samples compressed at different strain rates in 0.1 strain increments.

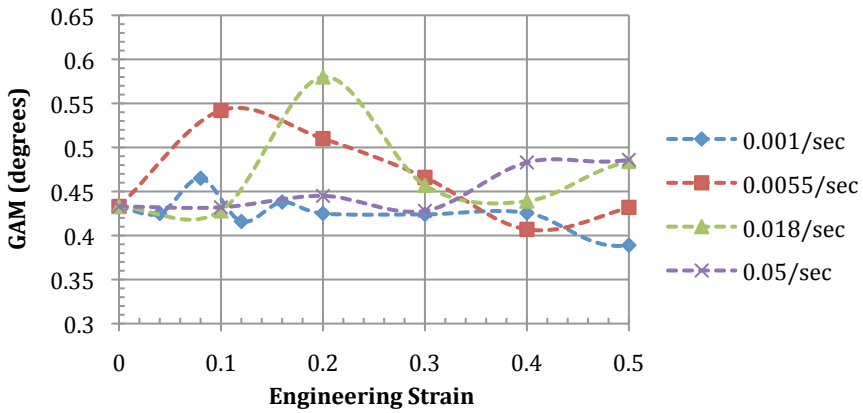

Figure 6.29: Average KAM of René 88DT samples compressed at different strain rates in 0.1 strain increments.

Figures 6.30 – 6.33 show the accumulation of grain average misorientation as a function of grain size for samples compressed at increments of **e** = 0.1 for different strain rates. During straining at 0.001/s, the average GAM as a function of grain size has a slight decrease as strain rate increases. As strain increases, the average GAM stays relatively constant. These trends are similar for samples strained at 0.0055/s. During straining at 0.018/s and 0.05/s, the average GAM for grains larger than 2μm increase as strain increases while average GAM of grains smaller than 2μm stay constant. The average GAM of the largest grains fluctuates unpredictably for all strains and strain rates. These grains are most likely the large grains that are a product of the extrusion process observed in chapter 3. These grains retain high degrees of misorientation from the extrusion process and this is retained through the simulated forging.

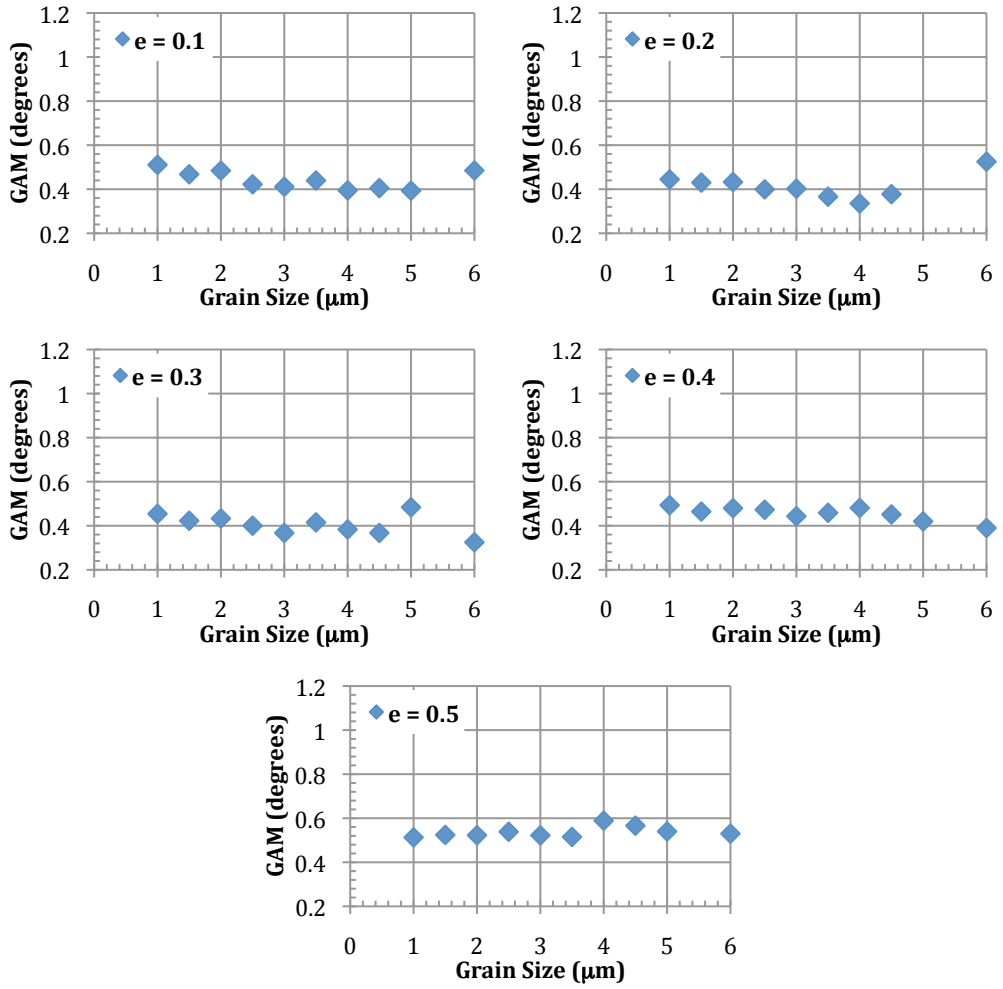

Figure 6.30: GAM as a function of grain size for René 88DT samples compressed at 0.001/s to e = 0.1 increments at 1298K (1025˚C).

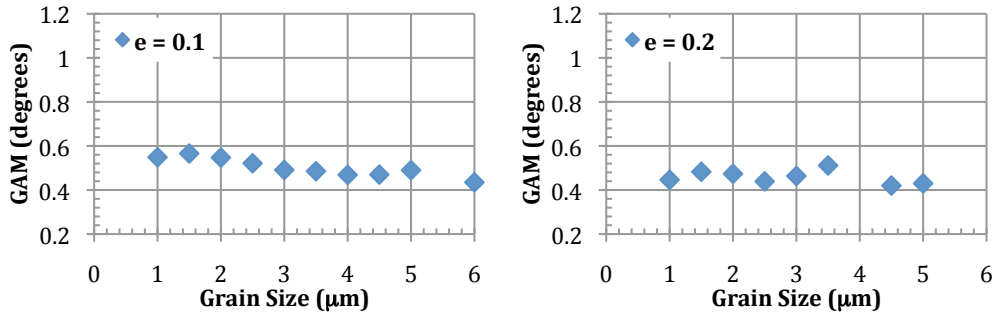

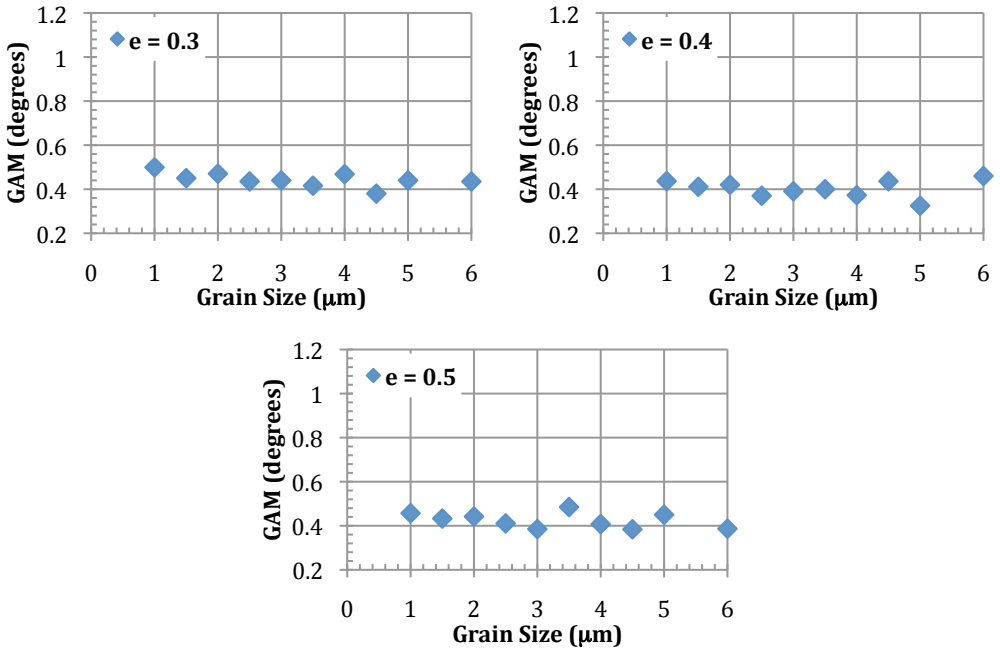

Figure 6.31: GAM as a function of grain size for René 88DT samples compressed at 0.0055/s to e = 0.1 increments at 1298K (1025˚C).

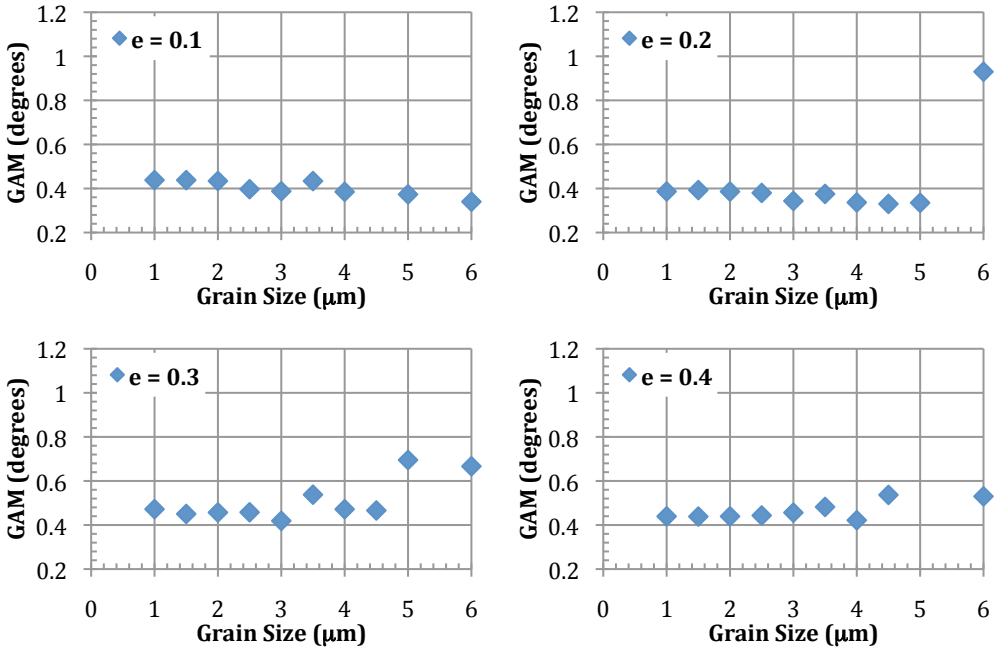

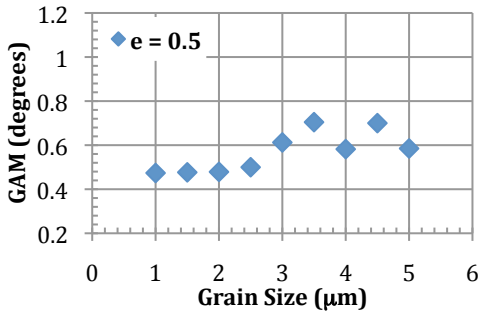

Figure 6.32: GAM as a function of grain size for René 88DT samples compressed at 0.018/s to e = 0.1 increments at 1298K (1025˚C).

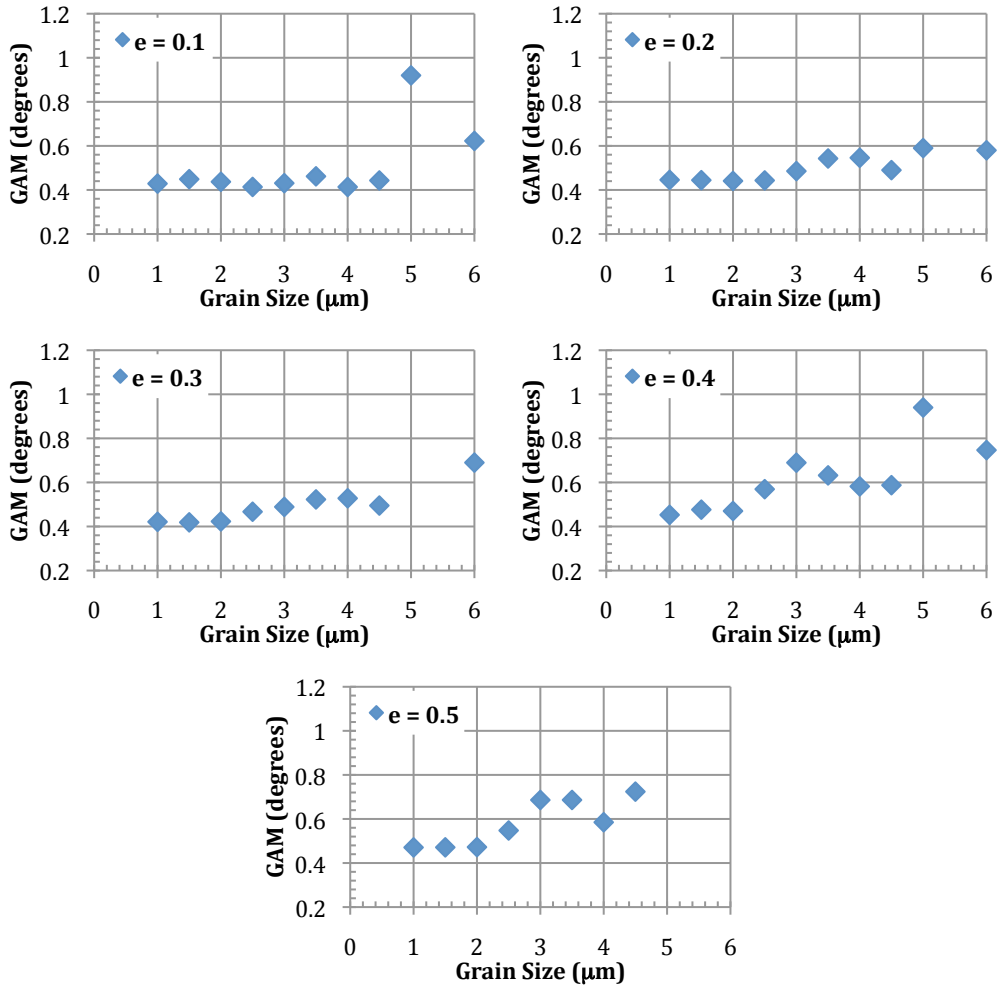

Figure 6.33: GAM as a function of grain size for René 88DT samples compressed at 0.05/s to e = 0.1 increments at 1298K (1025˚C).

6.4.2 Discussion

Analysis of the progression of GOS with incremental straining at 4 different strain rates during high temperature compression at 1298K (1025˚C) shows that at a

fully superplastic strain rate of 0.001/s, average GOS remains constant at ~0.43˚ with increasing strain, indicating that no transgranular misorientation is collected during deformation at 0.001/s. This is to be expected because grain boundary sliding is the dominant strain accommodation mechanism associated with superplastic flow. This observation is supported by the fact that both KAM and GAM show little increase as strain increases. Not only does little misorientation collect transgranularly during deformation at 0.001/s, but there is also a lack of grain size dependence in misorientation collected. All of the grains collect misorientation equally, with no population of grains accommodating more misorientation transgranularly than others.

During incremental straining at a strain rate of 0.0055/s, a strain rate within the transition deformation rates between superplasticity and power-law creep deformation, average misorientation increases at $\mathbf{e} = 0.1$ and then gradually decreases until $\mathbf{e} = 0.4$, at which point further deformation increases average misorientation at $\mathbf{e} = 0.5$. This trend in misorientation collected can be observed in GOS, KAM, and GAM data. The oscillation in collected misorientation indicates that dynamic recovery processes are occurring in an oscillatory manner. The most likely form of oscillatory dynamic recovery is dynamic recrystallization, where new grains nucleate after a critical amount of strain accumulates. Past studies have shown that oscillatory flow stress behavior during deformation of metallic materials during waves of dynamic recrystallization. The flow stress data for sample deformed at 0.0055/s does not show such oscillatory behavior. This most likely indicates that only a small fraction of grains are dynamically recrystallizing, not enough to substantially affect the macroscopic flow behavior of the material. Just like deformation at 0.001/s, there

is no grain size dependence of misorientation accumulation for samples deformed at 0.0055/s.

During incremental straining at 0.018/s, a strain rate just past the transition rates between superplasticity and power-law creep deformation, oscillation of collected misorientation is observed. But compared to the oscillation at 0.0055/s, the frequency of oscillation at 0.018/s is much higher; peaks in collected misorientation are $\mathbf{e} = 0.3$ apart, as shown by the GOS graph (Figure 6.27). This indicates that waves of recrystallization occur more frequently. But yet again, the flow stress curve shows no oscillating flow stress. Furthermore, the grain size dependence in misorientation accumulation is evident during deformation at 0.018/s. As strain increases, larger grains retain more misorientation as compared to the smaller grains. As discussed in the section 6.2.1.2, smaller grains are more superplastically favorable meaning that they are more likely to accommodate strain by grain boundary sliding. Therefore, less strain is expected to be accommodated transgranularly. By the same argument, larger grains are less likely to accommodate grain boundary sliding, therefore accumulating the majority of strain transgranularly, and increasing the measured misorientation.

During incremental straining at 0.05/s, a strain rate where René 88DT is expected to deform fully by power-law creep and where, as seen in chapter 5, high amounts of dynamic recrystallization is expected to occur, GOS, GAM, and KAM increase as the strain increases. However, no oscillation of accumulated misorientation is observed during incremental straining, indicating dynamic recrystallization. Nevertheless, the gradual grain refinement is evidence of dynamic recrystallization that occurs during deformation. The lack of oscillating transgranular

misorientation suggests that at this high strain rate, dynamic recrystallization has reached a steady state in that instead of waves of nucleation, dynamic recrystallization occurs at a constant rate as a function of strain. As strain increases, the amount of misorientation collected within the larger grains (D > 2μm) increases while the misorientation collected within smaller grains stays relatively constant. This grain size dependence is seen for samples compressed at 0.018/s and occurs by the same mechanism. In addition, the misorientation measured in the smaller grains may be less also because those are the dynamically recrystallized grains, which would have little strain accumulated.

6.5 Chapter Summary

In this chapter, measured misorientation measured by EBSD has been analyzed as a function of temperature, strain rate, and strain during high temperature compression of René 88DT. Several different types of misorientation measurements were used, including GROD, GOS, KAM, GAM, as well as GAM distributions. It is observed that misorientation accumulation differs within 3 different regimes of deformation: 1.) at slow strain rates, superplastic deformation by grain boundary sliding dominates 2.) at high strain rates, power-law creep deformation by transgranular strain accommodation dominates 3.) at intermediate strain rates, strain is accommodated by a combination of superplasticity and power-law creep that is grain size dependent. Observations regarding the spatial and temporal evolution of misorientation during superplastic deformation (at slow strain rates and higher temperatures) can be summarized as follows:

1. Little transgranular misorientation accumulates during superplastic deformation.
2. The Log-Lorentz fits of GAM distributions have small standard deviations and distribution peak parameter, meaning a narrow distribution width and low distribution peak value, respectively. However, the Log-Lorentz distribution fits have high amplitude.
3. Measured misorientation remains low at all strain intervals.
4. Measured grain average misorientation is not grain size dependent.

Deformation occurs by power-law creep deformation at high strain rates, and in this regime misorientation accumulation can be characterized as follows:

1. High average GOS, KAM, and GAM are observed during power-law creep deformation.
2. The Log-Lorentz fits of the GAM distributions have large standard deviations and low amplitude. The Log-Lorentz position parameter increases as a function of strain rate, which fits a power-law solution.
3. The measured misorientation steadily climbs as strain increases.
4. Larger grains accumulate more misorientation as strain increases.

During deformation at intermediate strain rates where a combination of power-law creep and superplasticity is expected to occur, misorientation accumulation is characterized as follows:

1. Measured average GOS, KAM, and GAM increase as a function of strain rate.

2. The Log-Lorentz fits of the GAM distributions have increasing standard deviation and a decreasing amplitude as strain rate increases. But the distribution peak parameter stays constant.
3. Misorientation measured as a function of strain rate oscillates with a frequency that increases with increasing strain rate.
4. Large grains accumulate more misorientation than smaller grains as strain increases, though the magnitude of the misorientation difference is smaller than fast strain rates where power-law creep dominates.

The analysis and characterization of misorientation accumulation during high temperature deformation gives a clearer understanding of the influence of strain and strain rate on grain structure evolution in René 88DT during high temperature hot working. The quantification of misorientation accumulation can lead to predictions of initiation and magnitude of dynamic recrystallization during deformation, which will be addressed in the next chapter. The ability to characterize misorientation accumulation during deformation also motivates a model for creep deformation that considers the transition from superplastic to power-law creep deformation.

Chapter 7

Deformation Mechanism Models

7.1 Superplasticity Enhanced Grain Growth

In Chapter 5, experiments on grain size evolution during superplastic deformation demonstrated some degree of grain growth. Many researchers have suggested that superplasticity enhanced grain growth (SEGG) occurs during high temperature deformation of metallic systems [16, 29, 66, 67]. But as discussed in Chapter 2, there are disagreements about the mechanisms for SEGG. In this chapter, we will propose a model for superplasticity-enhanced grain growth, which is applicable for both single and multi-phase metallic systems assuming that the driving force for grain growth is the reduction of grain boundary curvature.

7.1.1 Grain Growth with Zener Drag

In this proposed model of superplasticity-enhanced grain growth, which has been developed collaboratively with E. Payton at the Ohio State University, grain growth is proposed to occur by the same mechanisms as normal grain growth; grain coarsening is driven by reduction of boundary curvature. Therefore, grain growth rate, $\dot{d}$, is given by:

$$\dot{d} = M \cdot F \qquad [7\text{-}1]$$

where M is the grain boundary mobility and F refers to the driving force to reduce boundary curvature, usually given by:

$$F = \frac{2\gamma_b}{d} \qquad [7\text{-}2]$$

where γ_b is the grain boundary energy and d is the average grain size. When modeling normal grain growth of two-phase alloys, the influence of secondary particles is incorporated into the driving force for growth. The pinning force of secondary particles is derived from the Zener drag force (Z) created by the secondary particles on the grain boundaries, which is classically approximated by $Z = 2f_v/2r$. Therefore, the driving force for grain growth is given by:

$$F = \gamma_b\left(\frac{2}{d} - \frac{3f_v}{2r}\right) \qquad [7\text{-}3]$$

where f_v is the volume fraction of the secondary particles and r is their radius. This approximation for two-phase systems assumes that secondary particles are sparsely populated along the grain boundaries; However with René 88DT, this assumption is not valid, since γ' particles consist of between 14 – 43% of the volume fraction (V_f). When dealing with large volume fraction of particles such as in René 88DT, a relationship proposed by Humphreys and Hatherly gives a good estimation of the drag force (Z) of the secondary particles:

$$Z = \pi r\gamma_b\left(\frac{2}{d^2} + \left(1 - \frac{1}{N_v d^3}\right)2N_v r\right) \qquad [7\text{-}4]$$

where d and r are the diameter of the γ and the radius and γ' grains, respectively. N_v is the number of γ' particles per unit volume, and D is the diffusivity. Adding this drag force to the driving force for grain growth results in the following solution:

$$F = \gamma_b \left(\frac{2}{d} - \frac{\pi r}{d^2} + \left(1 - \frac{1}{N_v d^3} \right) 2 N_v r \right) \quad [7\text{-}5]$$

where N_v can be defined as:

$$N_v = \frac{3V_f}{4\pi r^3} \quad [7\text{-}6]$$

7.1.2 Atomic Diffusivity

In this study, grain boundary mobility will be averaged for a given thermodynamic condition, given by:

$$\overline{M} = \frac{A^2 V_m D_A}{\delta R T} \quad [7\text{-}7]$$

such that D_A is the intrinsic diffusion coefficient for nickel. The parameter δ is the grain boundary width, V_m is the molar volume of atoms in the material, R is Boltzmann's constant in J/mol/K, T is the temperature and A is a material constant. As discussed in Chapter 2, Clark and Alden proposed that during superplastic deformation, grain boundary sliding increases the boundary mobility due to increased atomic diffusivity in the vicinity of the grain boundaries. Resistivity experiments suggest that this phenomenon occurs because excess vacancies are created at the grain boundaries during deformation [66]. Therefore, the total atomic diffusivity D_A is the sum of the equilibrium atomic diffusivity D_A^{eq} and excess atomic diffusivity from excess vacancies D_A^s, given by the following equations [2]:

$$D_A^{eq} = D_0 \exp\left(-\frac{Q_s}{RT} \right) \quad [7\text{-}8]$$

$$D_A^s = D_A^{eq} X_v^s \exp\left(\frac{\Delta G_f}{RT} \right) \quad [7\text{-}9]$$

$$D_A = D_A^{eq}\left[1 + X_v^s \exp\left(\frac{\Delta G_f}{RT}\right)\right] \quad [7\text{-}10]$$

where D_0 is a constant related to the jump distance, Q_s is the activation energy for self-diffusion, and ΔG_f activation energy for vacancy formation. As measured for pure Ni, Q_s = 279.7 KJ/mol and D_0 = 190x10^{8}μm^2/s [68] and ΔG_f = 1.9eV [30]. The quantity X_v^s is the excess vacancy concentration created near the grain boundaries during grain boundary sliding that is associated with superplastic deformation. Clark and Alden describes a simple model for X_v^s as a function of strain rate and annealing rate of vacancies, which yields a solution that follows an Avrami-type equation in the form of:

$$X_v^s = \frac{K_1}{K_2}\dot{\varepsilon}\left(1 - \exp\left(-K_2 t\right)\right) \quad [7\text{-}11]$$

where K_1 is a constant such that $K_1\,\dot{\varepsilon}$ is the rate of vacancy creation, and K_2 is an unitless constant dependent upon the nature of the vacancy sinks. The solution proposed by Clark and Alden suggests that the creation of vacancies is time and strain rate dependent. However, experimental measurements of vacancy concentration suggest that the creation of vacancies is strain dependent rather than time dependent because the magnitude of grain boundary sliding is a function of strain, therefore, an more accurate form of X_v^s is:

$$X_v^s = \frac{K_1}{K_2}\dot{\varepsilon}\left(1 - \exp\left(-K_2'\varepsilon\right)\right) \quad [7\text{-}12]$$

where K_2' is a constant dependent upon vacancy relaxation, which has been reported to be close to unity [29]. The evolution of X_s^v as a function of strain at different superplastic strain rates is shown in Figure 7.1. As it can be seen, the saturation

vacancy concentration is reached at the same strain for all superplastic strain rates (ε~0.3).

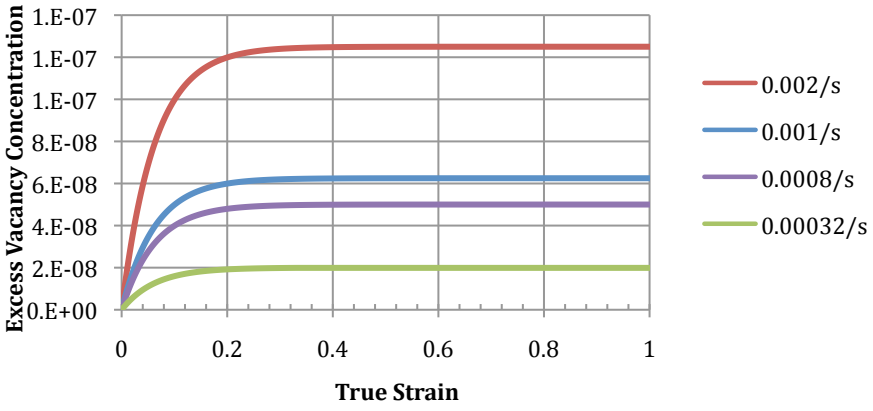

Figure 7.1: Excess vacancy concentration created near the grain boundaries during grain boundary sliding as a function of strain for various strain rates.

The enhancedment of atomic diffusivity near the grain boundaries as a function of strain for different superplastic strain rates for deformation at 1298K (1025˚C) is shown in Figure 7.2. The total atomic diffusivity D_A increases linearly with excess vacancy concentration and increases by 4x for the fastest superplastic strain rates. However, for the slowest strain rate tested (0.00032/s), the atomic diffusivity only increases by 50%.

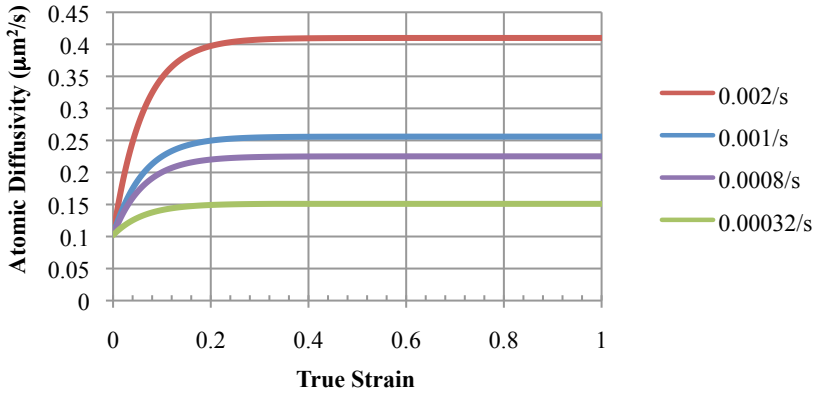

Figure 7.2: Atomic diffusivity as a function of strain for various superplastic strain rates at 1298K (1025˚C).

D_A as a function of strain for different temperatures at 0.001/s strain rate is shown in Figure 7.3. The equilibrium atomic diffusivity (D_A^{eq}) before deformation increases

with increasing temperature. The magnitude of the increase of the total atomic diffusivity (D_A) also increases as temperature increases due to change in vacancy concentration. Despite the independence of excess vacancy concentration, X_v^s from temperature, its effect on D_A increases as temperature increases.

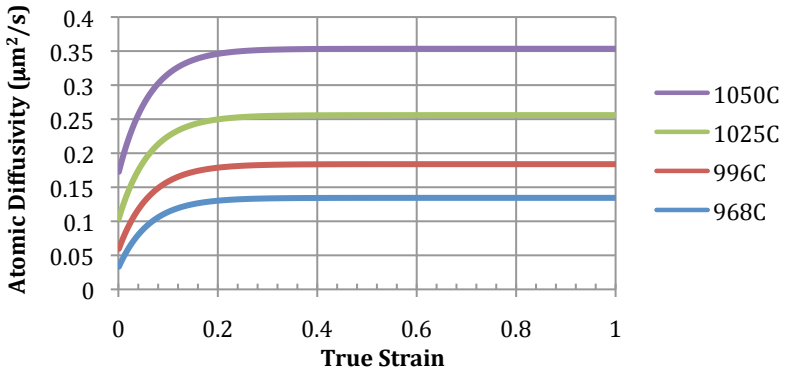

Figure 7.3: Atomic Diffusivity of René 88DT during deformation at 0.001/s at various temperatures as a function of true strain.

7.1.3 Model Grain Growth Predictions

Combining the solutions for grain boundary mobility and Zener drag forces for grain growth, time evolution of grain sizes can be calculated during superplastic deformation. Figure 7.4 shows the normalized grain size (d/d_o where d_o is the grain size before deformation begins) as a function of time for deformation at various strain rates for René 88DT deformed at 1298K (1025˚C). The initial average size ratio of γ' to γ is assumed to be 1:3. The figure shows that as strain rate increases, the initial grain growth rate increases. But as grain size reaches the critical Zener pinned grain size, the grain growth rate decreases until it reaches zero when the γ reaches Zener pinned level, which is 1.35x the initial grain size.

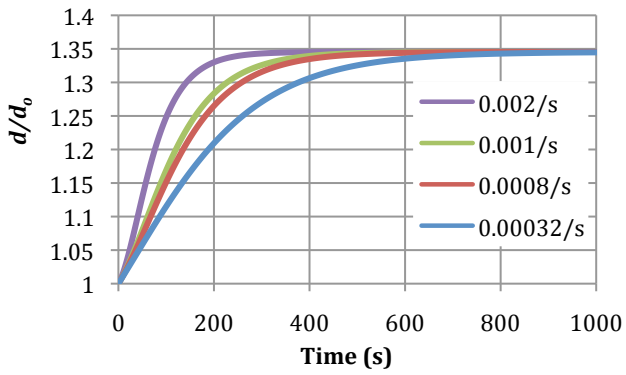

Figure 7.4: Grain diameter ratio of initial to current as a function of time for René 88DT deformed at various superplastic strain rates at 1298K (1025˚C).

Figures 7.5 and 7.6 compare the model predicted grain size ratio to experimentally measured grain size ratio of grains containing twins for samples deformed at 0.001/s and 0.002/s, respectively, both at 1298K (1025˚C). The figures shows that the proposed superplasticity enhanced grain growth model can be used to predict grain growth at superplastic strain rates. However, at strain rates where a combination of superplastic and power-law deformation occurs, the SEGG model does not accurately predict grain size evolution.

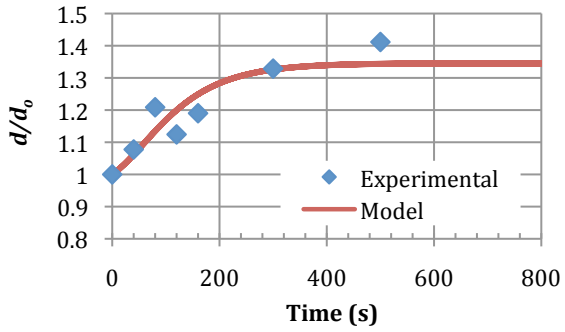

Figure 7.5: Grain diameter ratio of initial to time dependent grain size as a function of time for René 88DT deformed at 0.001/s at 1298K (1025˚C).

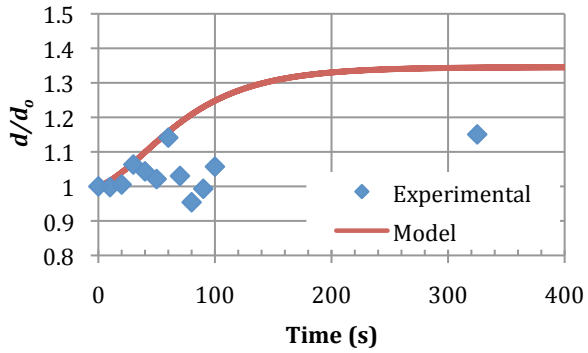

Figure 7.6: Grain diameter ratio of initial to time dependent grain size as a function of time for René 88DT deformed at 0.002/s at 1298K (1025˚C).

7.1.4 Discussion

In this section, a model for superplasticity enhanced grain growth (SEGG) has been proposed. The mechanisms by which grain growth occurs during superplasticity are logically the same as normal grain growth. But it is proposed that during superplastic deformation, grain boundary sliding increases the atomic diffusivity near the grain boundaries. Experimental comparisons to model predictions show that at fully superplastic strain rates, the model accurately predicts grain size evolution during deformation. However, when deformation mechanisms deviate from superplasticity, the model cannot account for the change in deformation mechanism and does not accurately predict grain growth.

Analysis of grain growth rates during superplastic deformation at various strain rates using the SEGG model shows that initial grain growth rates vary as a function of strain rate. However, as the grain size approaches the Zener-pinned maximum grain size, the grain growth rates decrease dramatically at all strain rates. The maximum difference in grain size ratio (d/d_o) for samples deformed at 0.001/s and 0.00032/s at 1298K (1025˚C) occurs at 200s and is only 10%. Therefore, it has been shown that although SEGG is predicted to occur, the effects are minimal due to

the microstructural stabilizing effects of the high volume fraction of γ' during forging. However, superplasticity-enhanced grain growth is predicted to have a much stronger influence on grain structure evolution at higher forging temperatures.

7.2 Boundaries of Superplasticity

Experimental measurements of flow stress, grain size, and EBSD misorientation show that the operational range for fully superplastic flow in René 88DT is temperature and strain rate dependent. The standard constitutive model for superplastic deformation, as discussed in chapter 2, is one that assumes a primary role for grain boundary sliding:

$$\dot{\varepsilon} = A\frac{D_{gb}\delta Gb}{kT}\left[\frac{b}{d}\right]^2\left[\frac{\sigma}{G}\right]^2 \qquad [7\text{-}13]$$

where $\dot{\varepsilon}$ is the strain rate, A is a constant, D_{gb} is the grain boundary diffusion coefficient, G is the shear modulus, b is the Burger's vector, d is the average grain size, σ is the flow stress, δ is the grain boundary width, T is the temperature, and k is the Boltzmann constant. As equation 7-13 shows, not only are the imposed deformation parameters (strain rate and temperature) important in determining superplasticity, but the microstructure is important as well. And as EBSD grain size data from chapter 5 shows, there is significant evolution of microstructure during high temperature deformation of René 88DT. Therefore, the superplasticity regime is not only strain rate and temperature dependent, but also grain size dependent.

7.2.1 Grain Boundary Diffusion Coefficient

When using equation 7-13, determination of the grain boundary diffusion coefficient is particularly difficult because it is an ill-defined parameter

experimentally. Because the movement of the grain boundary necessitates transport of atoms along and across the grain boundary, the most logical and agreed upon definition of D_{gb} is the atomic diffusion coefficient of atoms along the grain boundary. Therefore, D_A as defined by equation 7-10 is the closest measure of grain boundary diffusion coefficient during superplastic deformation. And as derived, D_A is a function of not only temperature, but also strain rate and strain due to excess vacancy creation at the grain boundaries during grain boundary sliding.

7.2.2 Analysis of Experimental Data

Equation 7-13 can be used to analyze experimental data of grain size and flow stress of René 88DT samples compressed at different strain rates and temperatures to determine boundaries of superplasticity.

$$\ln\left(\frac{\sigma}{G}\right)^2 = \ln\left[\frac{\dot{\varepsilon}kTd^2}{AD_A\delta Gb^3}\right] \qquad [7\text{-}14]$$

Equation 7-14 is plotted for all samples compressed at various temperatures and strain rates for ε = 0.7 in Figure 7.7. When experimental data follows the linear relationship with a slope of 1, the equation for superplastic deformation is satisfied indicating that deformation at that particular strain rate and temperature is superplastic. When the experimental data deviates from the line of superplastic behavior, other deformation mechanisms are operating.

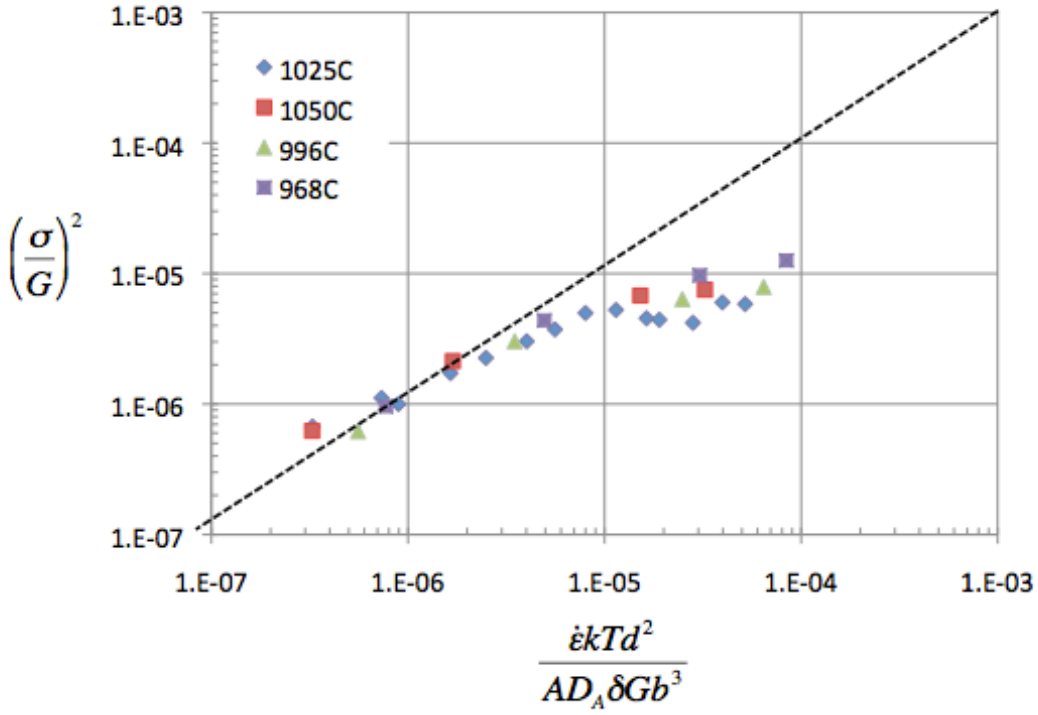

Figure 7.7: Plot of normalized flow stress vs. normalized grain size, temperature, and strain rate showing deviation of experimental data from solution, which satisfies superplastic deformation.

For René 88DT, experimental results show that superplasticity is the primary deformation mechanism if:

$$\ln\left[\frac{\dot{\varepsilon}kTd^2}{AD_A\delta Gb^3}\right] < -12 \qquad [7\text{-}15]$$

for experimental temperatures between 1323K (1050˚C) and 1241K (968˚C), and the constant $k/A\delta D_0 b^3 = 2\text{x}10^{14}$ J/K/μm^2/s, where D_0 is the intrinsic diffusivity described in section 7.1.2. Figure 7.8 shows the boundary of superplasticity as a function of grain size, temperature, and strain rate. The area below the 3D surface is where superplasticity is the dominant deformation mechanism during compression.

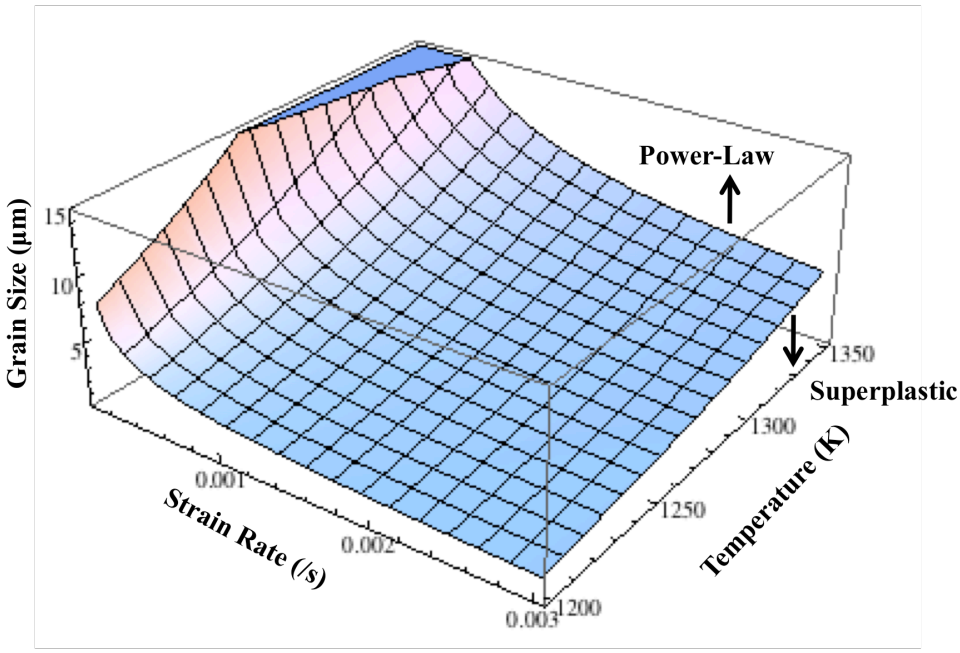

Figure 7.8: Boundaries of superplasticity as a function of grain size, strain rate, and temperature. The area below the 3D surface is where superplasticity dominates.

7.2.3 Discussion

As Figure 7.8 shows, the maximum superplastic grain size decreases by an order of magnitude when strain rate increases from 0.00032/s to 0.0032/s. Temperature has a comparably dramatic effect on maximum superplastic grain size; as temperature increases from 1241K (968˚C) to 1323K (1050˚C), the maximum superplastic grain size increases an order of magnitude. It is clear that not only does temperature and strain rate affect deformation mechanisms, but that grain size is also a determining variable of the deformation mechanism during high temperature compression. However, as grain size data reported in chapter 5 show, there is a distribution of grain size for the as-extruded and as-forged material. The non-uniformity of the grain size of the material will dramatically affect the local deformation mechanisms. As discussed in the next section, the maximum superplastic grain size as a function of temperature and strain rate can be used in conjunction with

measured grain size data to determine the fraction microstructure in which deformation by superplasticity and power-law creep occurs.

7.3 Deformation Mechanisms by Grain Fraction

It has been shown in section 7.2 that deformation mechanisms during high temperature compression of René 88DT are grain size dependent at a constant strain rate and temperature. The maximum superplastic grain size (d_{max}) can be calculated for each strain rate and temperature using equation 7-15. The d_{max} as a function of strain rate at various temperatures is plotted in Figure 7.9. As the figure shows, d_{max} changes by 2 orders of magnitude between 1/s and 0.0001/s.

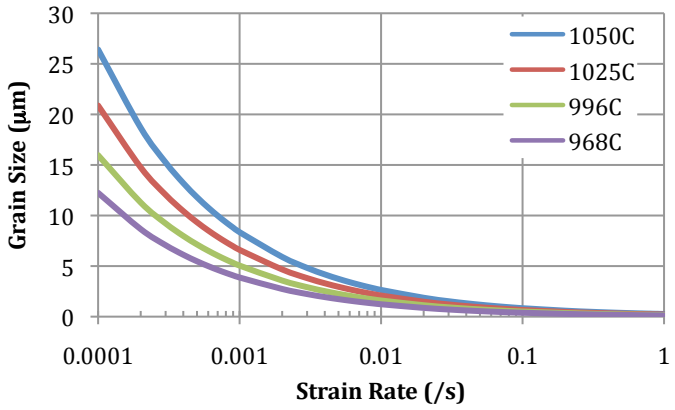

Figure 7.9: Maximum superplastic grain size as a function of strain rate for René 88DT deformed at René 88DT.

By using the calculated d_{max}, fraction of grains that deform non-superplastically can be counted from the EBSD collected grain size data for samples deformed at various strain rates. Figure 7.10 shows fraction of grains above d_{max} for samples compressed at various strain rates at 4 different test temperatures. The fraction of grains above d_{max} increases as compression temperature decreases, indicating that more of the microstructure is deforming by power-law creep. At higher compression temperatures, more of the microstructure is deforming superplastically when strain

rate is held constant. The maximum change in fraction of grains above d_{max} as temperature goes from 1323K (1050˚C) to 1241K (968˚C) is at 0.032/s, where the fraction increases from 0.4 to 0.93 respectively.

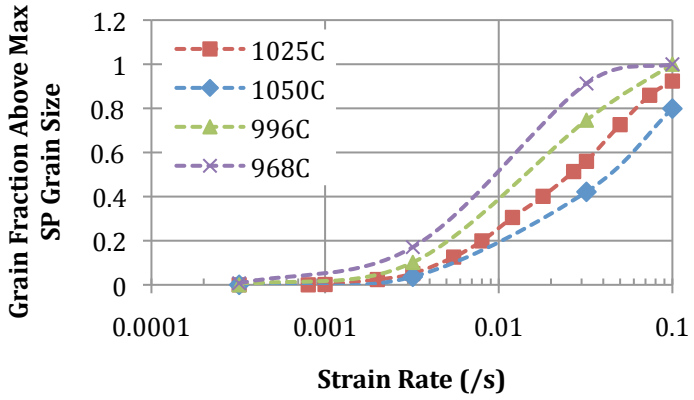

Figure 7.10: Fraction of grains above maximum superplastic grain size for samples deformed at various strain rates at various temperatures.

Figure 7.11 shows the fraction of grains above d_{max} as a function of strain for 4 different strain rates at 1298K (1025˚C). The figure shows that fraction of grains above d_{max} does not decrease significantly with strain at higher strain rates, indicating that dynamic recrystallization does not affect the fraction of grains that deform by superplasticity and power-law creep.

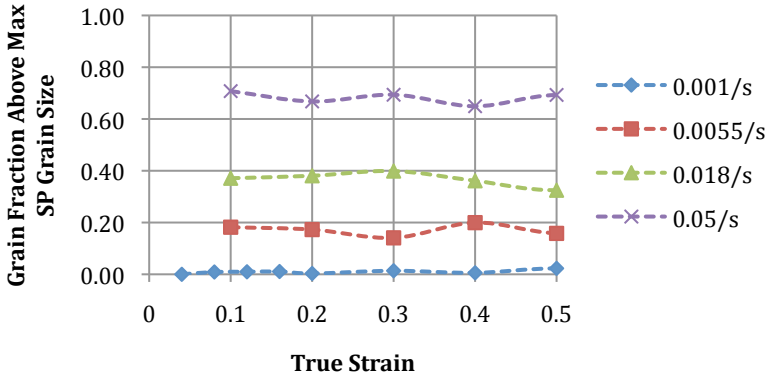

Figure 7.11: Fraction of grains above d_{max} as a function of strain for 4 different strain rates at 1298K (1025˚C).

Since deformation mechanisms can be classified for individual grains by their grain size, the average misorientation of grains deforming by superplasticity and power-law

creep can be separated. Figure 7.12 shows the average GAM of superplastic grains and power-law creep grains for samples deformed at various strain rates at 1298K (1025˚C) after an imposed true strain of 110%. The figures show that there is little correlation between predicted deformation mechanism and average grain misorientation.

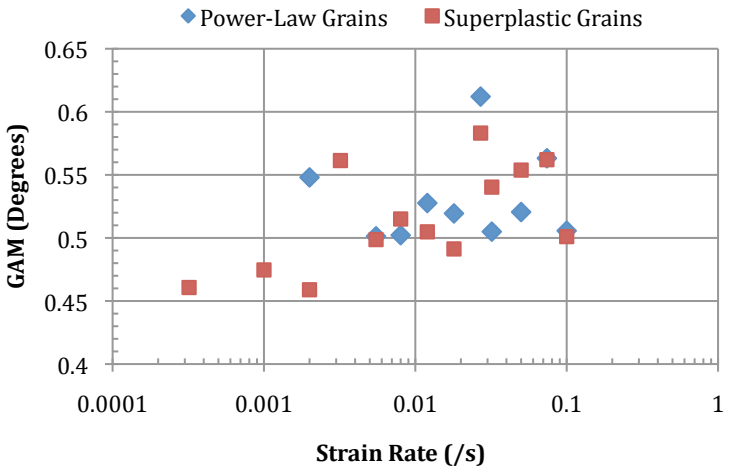

Figure 7.12: Average GAM of power-law creep grains and superplastic grains as a function of strain rate for René 88DT deformed to 110% true strain at 1298K (1025˚C).

7.3.1 Discussion

In this section, d_{max} is used to determine the fraction of the René 88DT microstructure that deforms by superplasticity and power-law creep. By determining deformation mechanism as a function of grain size, the deformation at intermediate strain rates, where mixed modes of deformation mechanisms exist, can be described. At those immediate strain rates, the large grains will deform by power-law creep while the smaller grains will deform by superplastic flow.

It has been shown that since d_{max} decreases by an order of magnitude as strain rate increases from 0.0001/s to 0.1/s, the fraction of microstructure that deforms by power-law creep increases significantly for the same range of strain rates. But

interestingly, when comparing the fraction of grains above d_{max} at various imposed strains, it stays constant as a function of strain at all strain rates. This suggests that at high strain rates, even the sizes of the dynamically recrystallized grains are larger than d_{max}. Therefore grains that have dynamically recrystallized do not deform by superplasticity after recrystallization, as some researchers have suggested [35].

Figure 7.12 showed the average GAM for René 88DT compressed at different strain rates, to the same strain. Though it is expected that power-law creep deforming grains would have higher transgranular misorientation than superplastic grains, EBSD scans revealed no correlation between deformation mechanism and accumulated GAM. Several factors could have contributed to this: 1.) dynamic recovery mechanisms during deformation at higher strain rates decreases the measured misorientation in power-law creep grains and 2.) non-yielding γ' grains with little transgranular misorientation are averaged into the GAM, skewing the resulting data. These factors can lead to inaccurate representation of transgranular misorientation of fractions of grains during deformation.

7.4 Average Grain Size by Deformation Mechanism

By using d_{max} as the limiting grain size for superplasticity, EBSD data of grain size can be separated into two grain groups, the first being those where $d \leq d_{max}$, which are the grains that deform by superplasticity at a given strain rate and temperature. The second group of grains are those where $d > d_{max}$, which are the grains that deform by power-law creep. Once the grains have been separated, an average grain size for those grains that deform by superplasticity and power-law creep can be calculated. Figures 7.13 and 7.14 show the average grain size of grains

deforming superplastically and by power-law creep as a function of strain rate, respectively.

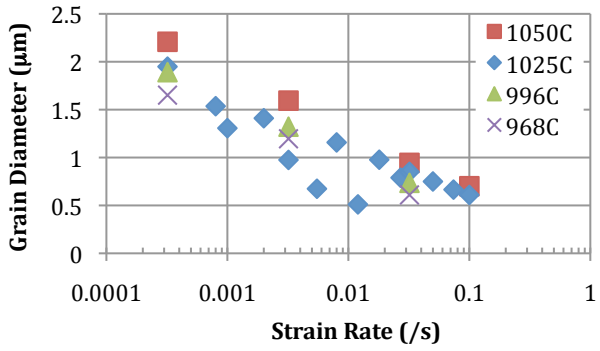

Figure 7.13: Average grain size of superplastic grains for René 88DT deformed at various strain rate at various temperatures.

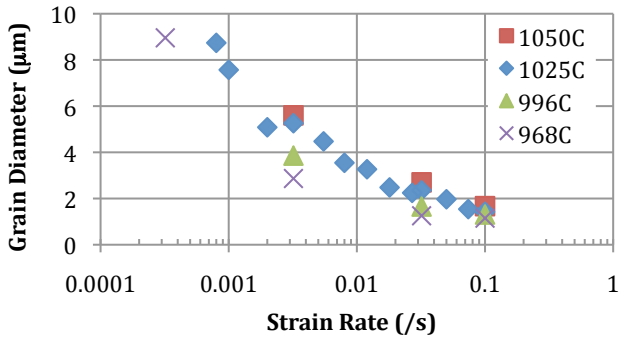

Figure 7.14: Average grain size of power-law creep grains for René 88DT deformed at various strain rate at various temperatures.

Figure 7.13 shows that the average grain size of the superplastically deforming grains decreases as strain rate increases; this is to be expected since d_{max}, the limiting grain size for superplasticity decreases significantly as strain rate increases. However, Figure 7.14 shows that there is significant grain refinement indicating dynamic recrystallization for grains that are deforming by power-law creep as strain rate increases. Dunne *et al.* suggested that the saturation grain size (d_s) for grain refinement by dynamic recrystallization as a function of strain rate follows the form [69]:

$$d_s = p\dot{\varepsilon}^q \exp\left(\frac{Q}{RT}\right) \quad [7\text{-}16]$$

where Q is the activation energy for recrystallization, q is the strain rate power coefficient, and p is a material constant. For best fit to René 88DT experimental data, assuming that ε = 1.1 is enough strain for the microstructure to reach saturation grain size, $p = 5x10^{-21}$, $q = 0.361$ and Q increases linearly with temperature so that $Q(J/mol) = 460.24T - 97388$. Using the this linear fit of Q for the given test temperature range, Q is close to 500kJ/mol, which is comparable to the activation energy measured for Ni-base superalloy at similar temperatures [70]. Figure 7.15 shows the d_s solution fit to power-law creep grain size data for samples compressed at 1298K (1025˚C). The progression of saturation grain size as a function of strain rate agrees with previous research suggesting that dynamically recrystallized grain size is inversely related to the strain rate [35, 71, 72].

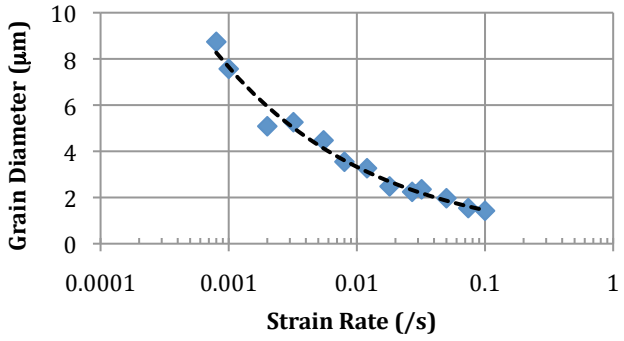

Figure 7.15: Average grain size of power-law creep grains for René 88DT deformed at various strain rate at 1298K (1025˚C) with saturation grain size solution fit.

7.5 Chapter Summary

In this chapter, models have been proposed to describe microstructural evolution during high temperature deformation of René 88DT. First, a mechanistic model for superplasticity enhanced grain growth (SEGG) was derived that is

applicable to for René 88DT, as well as any metallic system that deforms superplastically because the primary driving force for grain growth is, like normal grain growth, the reduction of boundary curvature. Furthermore, the model takes into account Zener drag forces due to secondary particles. While deriving SEGG, excess vacancy concentration (X_v^s) and total atomic diffusivity D_A are newly defined. Once grain growth during superplasticity is modeled, the boundary of superplasticity is analyzed using a mechanistic description of grain boundary sliding. It has been shown that not only is the operative regime for superplastic deformation determined by temperature and strain rate, but that grain size is also an important variable in determining the deformation mechanism of René 88DT. By determining the temperature and strain rate dependent maximum superplastic grain size (d_{max}), the experimentally collected René 88DT microstructure can be separated into fractions deforming by superplasticity and power-law creep. In the final section of this chapter, a mechanistic model to determine saturation grain size (d_s) was proposed to model the post-deformation average grain size of the fraction of the microstructure that deforms by power-law creep.

To summarize, using the models proposed in this chapter, it is possible to predict deformation mechanisms and grain size evolution of René 88DT during high temperature forging at temperatures between 1241K (968˚C) and 1323K (1050˚C) and at strain rates between 0.00032/s and 0.1/s.

Chapter 8

EBSD Misorientation and Dislocation Density

Dislocation density has always been a material characteristic of interest for prediction of material behavior. When analyzing deformation and dynamic recrystallization, dislocation density is a critical parameter in determining stored energy, deformation mechanisms, and dynamic recrystallization. Unfortunately, the only reliable way of measuring dislocation density has been by transmission electron microscopy (TEM). There are several undesirable characteristics of TEM analysis: TEM sample fabrication is tedious and time consuming. The useful sample volume for analysis is under $10\mu m^3$. Such small area of analysis makes any measurement of dislocation density highly dependent on local microstructure and may not be representative of the entire microstructure of the material. The EBSD technique has the potential as a new and better way to measure dislocation density when larger scale information is required that cannot be acquired by TEM. In this chapter, we will discuss the relationship between measured misorientation by EBSD and dislocation density and derive a simple but new method for characterizing dislocation density on the grain scale. The resulting EBSD-measured dislocation density will be compared to flow stress-correlated dislocation density and the validity of measuring dislocation density using EBSD will be discussed.

8.1 Relationship Between KAM and Dislocation Density

As described in chapter 6, KAM is the average misorientation magnitude of a scan point relative to its nearest neighbor points. If a regular pattern of EBSD scan points is represented by the dots shown in Figure 8.1, then the KAM of the red scan point is the average of the misorientation from its neighboring points, which the arrows point to.

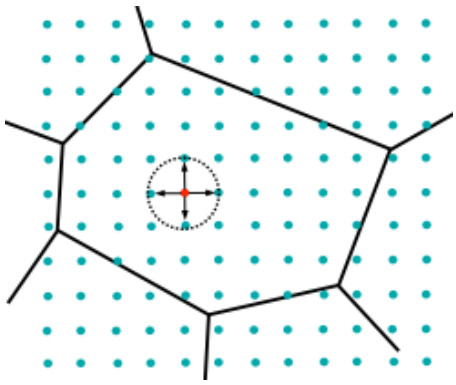

Figure 8.1: Regular pattern of EBSD scan points over representative microstructure. KAM of the red scan point is the average misorientation from its neighboring points.

The misorientation measured from the red scan point to one of its closest neighboring points is the measure of the lattice rotation in degrees. No rotation direction is assigned to the misorientation, therefore only the magnitude of the lattice rotation is known. For such a lattice rotation to exist, excess dislocations of the same Burgers vector need to be present between the scan points. A simple relationship between an array of edge dislocations and misorientation (θ) is shown in Figure 8.2.

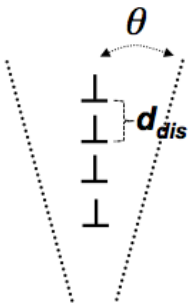

Figure 8.2: Schematic of relationship between an array of edge dislocations and lattice strain in degrees.

The relationship between θ in radians and the distance between dislocations in an array of edge dislocations (d_{dis}) is defined as:

$$\theta = \frac{b}{d_{dis}} \qquad [8\text{-}1]$$

where b is the Burgers vector. Therefore, if we assume that the lattice strain between two adjacent EBSD scan points is caused by an array of edge dislocations, the relationship between measured KAM and dislocation density (ρ) is:

$$\rho = \frac{4\frac{L_{sp}}{d_{dis}} K_{dl} \cdot d}{\pi \cdot L_{sp}^2 d} \qquad [8\text{-}2]$$

where L_{sp} is the distance between scan points, which in this case is the scan step size of 0.2μm. Since the distance between dislocations in an array is d_{dis}, then the average number of dislocations between two scan points is L_{sp}/d_{dis}. In equation 8-2, d is the grain size and K_{dl} is the out of plane dislocation length factor in relation to the grain size, varying between 0 and 1, making $K_{dl} \cdot d$ the average length of the dislocations. Since the dislocation density is calculated for a circular volume with radius = L_{sp}, the lattice misorientation in four directions are measured (the ±x and ±y directions) for a single value of KAM. This means that a total of 4 dislocation arrays, one in each measured direction, are present. Each dislocation array has a total dislocation length

of $L_{sp}K_{dl}d/d_{dis}$. Therefore, the combined dislocation length of all four dislocation arrays is $4L_{sp}K_{dl}d/d_{dis}$. When applying this model to René 88DT during deformation, d is held constant as the average as-extruded grain size. However, in reality, there is complex grain size evolution during strain as a function of strain rate and temperature. The volume of material that the dislocation density is measured is a cylinder with the radius of the scan step size (L_{sp}) and length of the grain size (d). Equation 8-1 and 8-2 can be combined and simplified to:

$$\rho = \frac{4K_{dl}\theta}{\pi L_{sp}b} \qquad [8\text{-}3]$$

The relationship between lattice strain (θ) in radians and the measured KAM (θ_{KAM}) in degrees is given by:

$$\theta = \frac{\pi\left(\theta_{KAM} - \theta_i\right)}{180} \qquad [8\text{-}4]$$

where θ_i is the correction parameter of measured KAM due to the resolution of the EBSD system. Experimental results KAM for as-extruded samples after aging show that the resolution of EBSD system is around 3.5° for the scan parameters mentioned in chapter 5. Therefore, $\theta_i = 3.5°$. However, scan time is unimportant, more accuracy can be obtained from the EBSD system if different binning and exposure time is used.

8.2 KAM Dislocation Density Calculations

Figure 8.3 shows the EBSD measured dislocation densities using equation 8-3, as a function of strain rate for René 88DT compressed to 1.1 true strain at 1298K (1025˚C). Due to the step size dependence of measured KAM, dislocation density is calculated from KAM for two different step sizes to determine step size effect on

dislocation density. As Figure 8.3 shows, the user determined step size does not affect the calculated dislocation density due to the fact that both the volume and the KAM measured scales with step size.

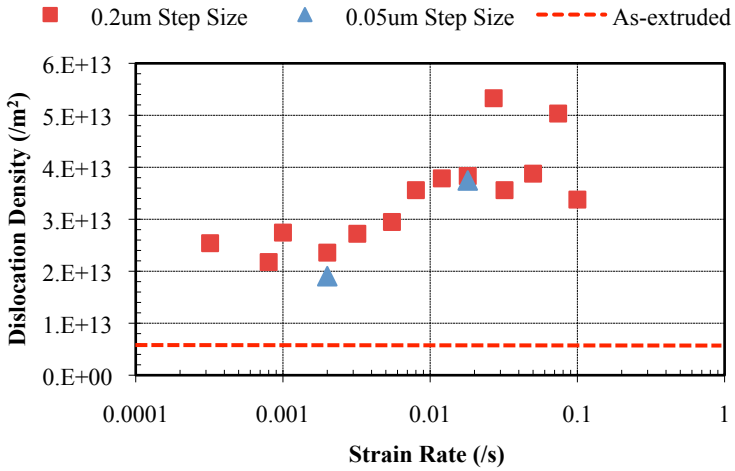

Figure 8.3: EBSD calculated dislocation density as a function of strain rate for René 88DT compressed to 1.1 true strain at 1298K (1025˚C). As-extruded dislocation density is indicated by red line.

The figure also shows that during deformation at slow superplastic strain rates, the average dislocation density is around $2.5x10^{13}/m^2$. As strain rate increases at intermediate strain rates, the dislocation density increases to around $4x10^{13}/m^2$ where it plateaus for high strain rates. The as-extruded dislocation density is $6.8x10^{12}/m^2$, which matches in magnitude to reported dislocation densities of soft annealed metallic crystals [73]. Carroll *et al.* reported a dislocation density for experimental single crystal blade superalloy UM-F20 after creep rupture at a rate of $1.5x10^{-5}/s$ and temperature of 1020˚C to be $3x10^{12}/m^2$ [74]. Pollock *et al.* showed single crystal blade superalloy CMSX-3 to contain about the same dislocation density after solution treatment and aging as well [75]. These results suggest that the dislocation densities measured using KAM are reasonable considering the high strain and strain rates imposed on the samples. The plateau in dislocation density at high strain rates may

indicate that some steady state dislocation density has been reached due to the combination of dislocation creation and annihilation due to dynamic recrystallization.

Figure 8.4 shows the EBSD-measured dislocation density as a function of strain rate for samples compressed to 1.1 true strain and at various temperatures. The figure shows that the accumulation of dislocation during deformation is temperature dependent at all strain rates. Higher dislocation densities were measured in samples compressed at lower temperatures. Though the figure shows this trend qualitatively, more measurements are needed to determine quantitative temperature dependent dislocation density.

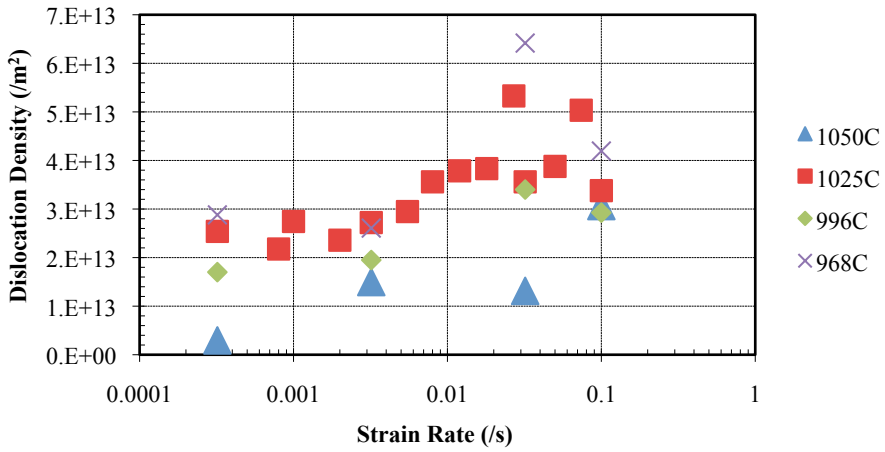

Figure 8.4: KAM calculated dislocation density as a function of strain rate for René 88DT compressed to 1.1 true strain at various temperatures.

8.3 Flow Stress Correlation Dislocation Density

In this section, EBSD-measured dislocation density will be compared to the flow stress-correlated dislocation density as defined by plasticity theories [76]. But before dislocation densities can be compared and discussed, the relationship between dislocation density and flow stress will be derived using constitutive plasticity theory. Since multiple strengthening mechanisms are operative, the contributions to the compressive yield stress are separated using the strength model for Ni-base

superalloys derived by Kozar *et al.* [77] to aid in determining the fraction of the strength contribution from dislocation-dislocation and dislocation-grain boundary interactions, independent of precipitate strengthening mechanisms.

8.3.1 Plasticity and Dislocation Density

Constitutive plasticity theory developed by Kocks and Mecking [76] is useful in relating plastic flow behavior to dislocation density in metallic systems. In this approach the average dislocation density ρ is considered the governing parameter for strain hardening. Therefore, the relationship between mechanical hardness from obstacles to dislocation glide $\hat{\sigma}$ and dislocation density can be described by:

$$\hat{\sigma} = M\alpha Gb\sqrt{\rho} \qquad [8\text{-}5]$$

where M is the average Taylor factor (3.06 for FCC crystal structure), α is a microstructural factor accounting for Hall-Petch effects, which is reported to be around 0.3 [78], b is the burgers vector, and G is the shear modulus. The quantity $\hat{\sigma}$ is defined operationally as the flow stress at a given dislocation density measured at "reference conditions" of defined temperature and strain rate $\dot{\varepsilon}_o$. The relationship between $\hat{\sigma}$ and stress contribution from dislocation interaction as a function of strain rate σ_{dis} is defined by a reorganized power-law solution [79]. Therefore the relationship between σ_{dis} and ρ at a given strain rate $\dot{\varepsilon}$ is given by:

$$\sigma_{dis} = M\alpha Gb\sqrt{\rho}\left(\frac{\dot{\varepsilon}}{\dot{\varepsilon}_o}\right)^{1/m} \qquad [8\text{-}6]$$

Furthermore, flow stress σ is defined as:

$$\sigma = \sigma_o + M\alpha Gb\sqrt{\rho}\left(\frac{\dot{\varepsilon}}{\dot{\varepsilon}_o}\right)^{1/m} \qquad [8\text{-}7]$$

where σ_o is the contribution to flow stress from solid-solution strengthening and dislocation-precipitate interactions, which is defined as [78]:

$$\sigma_{yield} = \sigma_o + \left(1 - f_{\gamma'}\right) k d_{\gamma}^{-\frac{1}{2}} + f_{\gamma'} k d_{\gamma'}^{-\frac{1}{2}} \qquad [8\text{-}8]$$

where σ_{yield} is the yield strength, and the two other contributions to σ_{yield} other than σ_o are the Hall-Petch effects of the γ and γ'.

8.3.2 Strengthening Contributions of René 88DT

Kozar *et al.* assessed the contributions of specific features of the microstructure of polycrystalline Ni-based superalloys to the overall strength of the material [77]. Solid-solution strengthening, Hall-Petch effects, precipitate shearing, and other dislocation-precipitate interactions were considered in the proposed strength model. The derivation of the Kozar strength model shown in detail [77] and will not be repeated here. When the René 88DT composition, γ and γ' volume fraction, and γ and γ' grain sizes are input into the strength model, solid solution strengthening and dislocation-precipitate interaction accounts for 50% of the total strength at test temperatures of interest in this research. Therefore the Kozar strength model suggests that $\sigma_o = 0.5\sigma_{yield}$.

8.3.3 Dislocation Density Comparisons

Figure 8.5 shows overlays the KAM calculated dislocation density with the flow stress correlated dislocation density for René 88DT compressed at 1298K (1025˚C) as a function of strain rate. The calculation of flow stress correlated dislocation density assumes that the microstructural constant related to Hall-Petch evolution stays constant during deformation at $\alpha = 0.265$. However, for more accurate

calculations of dislocation density, α would ideally be independently measured considering the grain size dependence of strength on both the γ and γ' phases. Despite the assumption of constant microstructure, the dislocation densities compare very well, showing the same trend of increasing dislocation density with increasing strain rate.

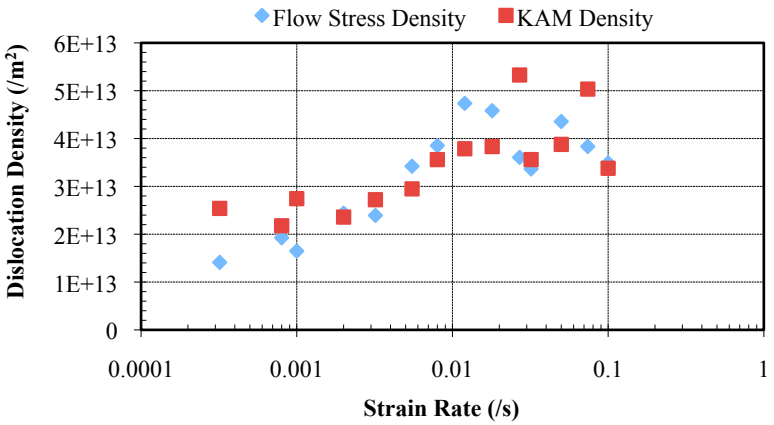

Figure 8.5: KAM calculated dislocation density compared to flow stress correlated dislocation density as a function of strain rate for René 88DT compressed at 1298K (1025°C).

At slow strain rates (<0.001/s), the dislocation densities deviate from each other. This is most likely due to the fact that strain rate sensitivity coefficent *m* in the plasticity model is held constant at experimentally measured 0.11 for power-law creep deformation. However, experimental results show that strain rate sensitivity increases as strain rate decreases into the superplastic deformation regime. Therefore, strain gradient plasticity model is not able to predict the dislocation density during superplastic deformation accurately. Nevertheless, the comparable magnitude and evolution of dislocation density with strain rate validates the magnitude of the dislocation density calculated using EBSD measured KAM.

8.4 Discussion

Using a simple relationship between dislocation arrays and lattice misorientation, EBSD data can be used to calculate dislocation density at the sub-granular scale. Comparison of EBSD calculated dislocation density with flow correlated dislocation density shows a good match in average dislocation density magnitude and trend as a function of strain rate. However, due to the derivation of dislocation density from lattice misorientation, neighboring dislocations of opposite Burgers vector that sum to zero lattice misorientation would not be counted into the dislocation density if the step size of EBSD scans is more than the distance between neighboring dislocations or if the local dislocations create misorientation that is below the EBSD resolution. In past studies, total dislocation density has been separated into two populations [32]. The first is those dislocations that account for misorientation within grains, referred to as "geometrically necessary dislocations" (GND). The second group of dislocations are "statically stored dislocations" (SSD), which are those neighboring dislocations that have opposing Burgers vectors and therefore do not contribute to the net misorientation of the grains. Because EBSD relies on lattice misorientation to measure dislocation densities, the dislocation densities that the EBSD measures are only for those dislocations that create lattice misorientation within the grains, which by definition are the GNDs. However, during deformation at high strain rates, SSDs create dislocation substructures, which are detected by EBSD, as seen in chapter 6. Therefore only the SSDs at slow strain rates and low strain are missed by the EBSD technique. Furthermore, studies have reported dislocation density for annealed nickel with little lattice misorientation, where

majority of dislocations would be SSDs, of at least one order of magnitude lower than the EBSD measured dislocation densities reported in this study [73].

8.4.1 Factors Affecting Dislocation Density Estimation

The accuracy of dislocation density calculated using KAM data could be improved if the accuracy of the orientation measured by EBSD is improved. First, the binning of the scan points can be reduced so that its neighbors do not affect each scan point orientation. However, the reduction in binning would increase the exposure time needed for each scan point to insure accuracy of collected Kikuchi patterns. Furthermore, since the substructure of dislocation content within grains varies depending on grain size, the step size of the EBSD scans should be decreased to increase the likelihood of capturing dislocation substructure in smaller grains. Both of these steps to increase accuracy of EBSD measure orientation would increase the time per scan. Keeping in mind that a reduction in scan step size by ½ would increase the scan time by 4x for the same area scan, it becomes a user determined trade-off between scan accuracy and scan time. The ultimate determining factor of course would be the grain size distribution of the microstructure scanned.

Chapter 9

Summary and Future Work

Characterization of microstructural evolution and strain storage during high temperature deformation of René 88DT has contributed a better understanding of the material response to high temperature superplastic forging during the thermo-mechanical processing of Ni-base superalloys. High temperature strain mapping was used to characterize strain accommodation on the super-granular scale during deformation. SEM EBSD technique was used to observe both the microstructural evolution and the strain storage evolution at the sub-granular level during high temperature deformation. The first objective of this study was to identify the deformation mechanisms during high temperature compression at simulated forging conditions. A combination of high temperature compression along with flow stress, strain mapping, and EBSD analysis showed that superplastic and power-law creep deformation mechanisms exist during high temperature compression and that the boundaries of the deformation mechanisms are temperature, strain rate, and grain size dependent. The second objective of this study was to characterize the evolution of grain structure during high temperature deformation. It was shown though EBSD grain size analysis that both the γ grains and the γ' particles evolve during and pre-deformation and that the evolution of both phases is dependent on deformation conditons. EBSD grain size analysis also showed that fraction of grains containing

twins correlates with the volume fraction of γ'. The third objective of this study was to quantify strain accommodation and storage at the grain scale during deformation. EBSD misorientation analysis gave clear indication of differences in strain accommodation and strain storage mechanisms for the two deformation regimes. Furthermore, a new technique to measure dislocation density by utilizing EBSD misorientation data was proposed. The final objective of this study was to model deformation mechanisms and the corresponding microstructural evolution during high temperature compression. By separating the two primary phases (γ and γ') and analyzing all microstructural phenomena that occur for both phases during high temperature deformation, a complete picture of the evolution of René 88DT microstructure was developed, along with models to describe this evolution. Figure 9.1 shows a flow chart for the integration of individual models developed to describe the complete René 88DT microstructure evolution during high temperature compression along with the section of the thesis where the modeling elements are described.

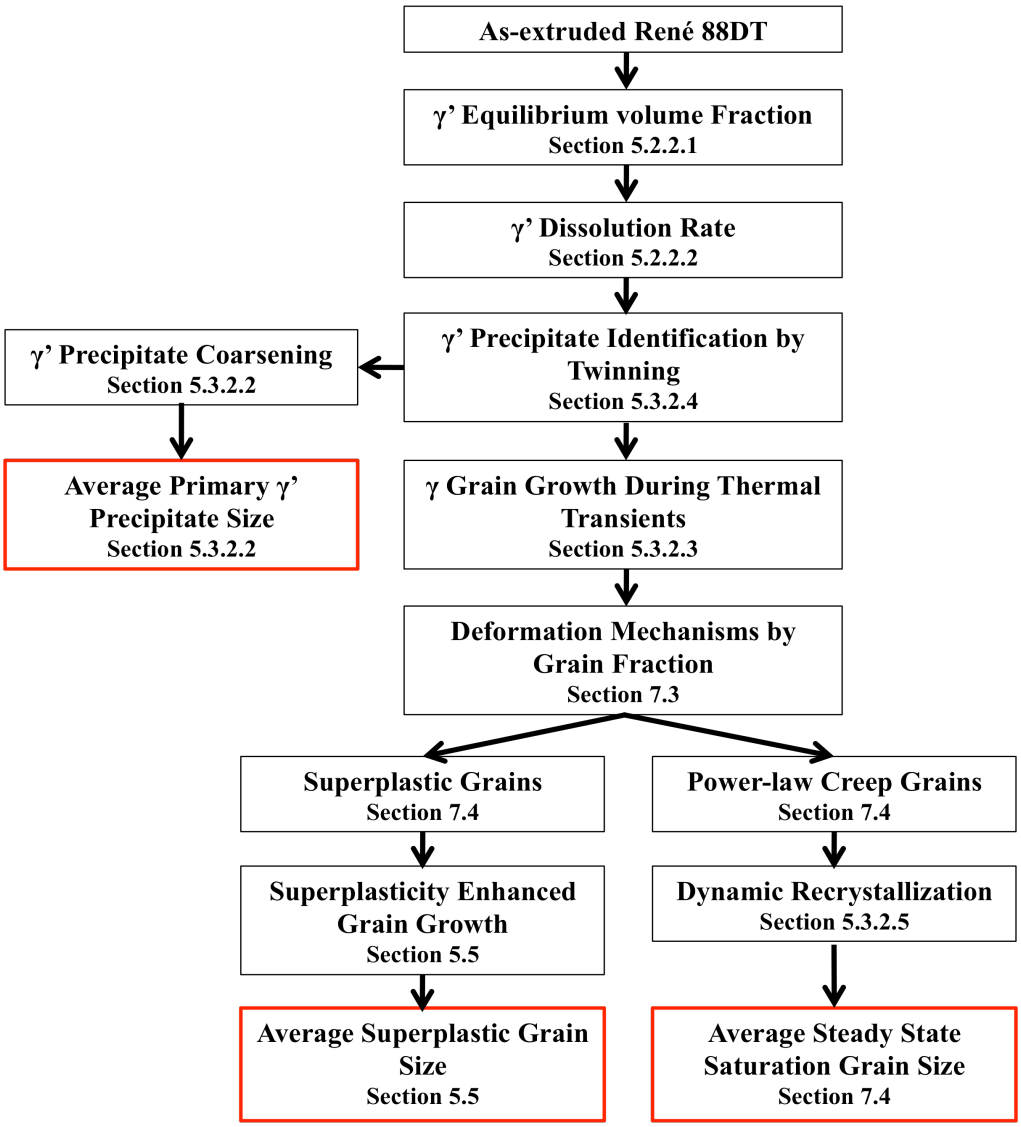

Figure 9.1: Flow chart describing the steps taken in the complete analysis of René 88DT microstructure evolution during high temperature compression along with the section it is described in this study. The final average grain size for each group of grains highlighted in red can be averaged to give a total average grain size for René 88DT post-deformation.

The flow chart shows that the first step in modeling René 88DT microstructure evolution is to determine the γ' equilibrium volume fraction during thermal transients pre-deformation and also during deformation. Once γ' equilibrium volume fraction is calculated, the γ' dissolution rate can be determined for test temperatures. The γ' dissolution rate is important in determining γ grain growth during and pre-deformation. Average γ' particle size is calculated during deformation by using the γ'

particle coarsening rate model. Deformation mechanisms for each γ grain are determined during deformation by using a critical grain size for superplastic deformation as a function of temperature and strain rate. Those grains that are smaller than the critical grain size deformation superplastically while the rest deform by power-law creep. Due to differing deformation mechanisms, each group of grains experience very different evolution. Superplastic grains experience enhanced grain growth, which is modeled by the superplasticity enhanced grain growth model. The power-law creep grains experience dynamic recrystallization and grain refinement during deformation. The steady state dynamically recrystallized grain size can be determined by using the strain rate and temperature dependent saturation grain size model. With the γ', superplastic, and power-law creep grain sizes predicted by separate models, the total René 88DT microstructure evolution has been described for high temperature compression at conditions that simulate high temperature forging. These models provide a clear understanding of the effects of high temperature forging on the structure of René 88DT and can be used to optimize forging conditions to obtain desired post-forging microstructure. Combined with characterization and models of microstructural evolution during high temperature heat treatments of the same alloy by E. Payton *et al.* [2], a better understanding of the entire thermo-mechanical processing of Ni-base superalloys and the relationship between processing and the final alloy microstructure is provided.

9.7 Future Work

Based on the findings of this study, the following recommendations are made for future investigation in this area.

1.) Experiments have shown that area fraction of grains containing twins correlates well with predicted volume fraction of γ'. Using a combination of phase identification analysis by Electron Diffraction Spectroscopy (EDS) and the grain orientation analysis by EBSD can determine which grains contain twins as well as the phase of each individual grain. In addition, combination of EDS and EBSD scans can determine the fraction of primary γ' that are coherent. Therefore, to accurately determine the twinned grain evolution of René 88DT during high temperature compression, a combination scans of EDS and EBSD on the same area of samples need to be completed for the same testing conditions as those carried out for this study.

2.) EDS and EBSD combination scans are also needed to verify the kinetics of γ' dissolution rate along with the coarsening rate of γ at high temperature before and during compression. It was assumed in this study that all of the twinned grains are γ grains during slow strain rate deformation. Therefore, the grain growth rates of γ were measured for those grains containing twins. Phase identification abilities of EDS would be invaluable in combination with EBSD to determine the grain growth and refinement rates of γ and γ' to compare with model predictions.

3.) The majority of EBSD scans in this research were completed with a step size of 0.2μm. However, more accurate identification of grain boundaries and grain misorientation substructure can be determined if the step size of EBSD scans were decreased to the resolution limit of the EBSD system in an field emission gun (FEG) SEM (0.02μm). Therefore, more accurate measures of grain size and transgranular

misorientation can be complete if the step size of EBSD scans can be decreased for all test conditions in this study.

4.) Although the evolution of microstructure and strain storage during high temperature compression at conditions chosen to simulate forging conditions was characterized, the effects of forging on microstructure evolution during subsequent thermo-mechanical processing were not studied. It is important to be able to understand the effects of forging conditions on the microstructure during subsequent heat treatments of René 88DT. Therefore, it is proposed that simulated heat treatments should be carried out on René 88DT samples after simulated forging and to use EBSD to characterize both the evolution of microstructure and also stored strain during post-forging heat treatments.

5.) Flow stress correlated dislocation density was used to compare to EBSD measured dislocation density in this study. However, to get a physical measure of dislocation density and to further validate the EBSD measured dislocation density, TEM analysis is needed. It is suggested that FIB lift-off techniques should be used to fabricate TEM samples from sample areas where EBSD scans have been complete. The TEM samples should be analyzed for dislocation content in an effort to determine local dislocation densities. The TEM observed dislocation density should be compared to EBSD measured dislocation densities in order to determine the accuracy of EBSD measurements of dislocation density.

6.) Although the saturation recrystallized grain size has been determined during deformation, it is only applicable once dynamic recrystallization has reached steady state. The evolution of grain size and the rate of dynamic recrystallization are still

unknown. However, by using the EBSD measured dislocation density technique to measure localized dislocation densities, a critical local dislocation density to trigger recrystallization nucleation can be determined and a full study of nucleation rates and dynamic recrystallization can be done. Therefore it is proposed that higher resolution EBSD scans be taken for samples compressed at power-law creep deformation rates with the goal of analyzing nucleation and growth of recrystallized grains.

References

[1] D. D. Krueger, R. D. Kissinger, R. G. Menzies, in: S. D. Antolovich, R. W. Stusrud, R. A. Mackay, D. L. Anton, T. Khan, R. D. Kissinger, D. L. Klarstrom (Eds.), 7th International Symp on Superalloys, Champion, Pa, 1992, pp. 277-286.

[2] E. Payton, Characterization and Modeling of Grain Coarsening in Powder Metallurgical Nickel-Based Superalloys, in: Materials Science and Engineering, vol Ph.D, The Ohio State University, Columbus, 2009.

[3] H. Fecht, D. Furrer, Advanced Engineering Materials 2 (2000) 777-787.

[4] J. Moll, McTiernan, BJ., Powder Metallurgy Superalloys, in: www.asminternational.org, ASM International, 2002.

[5] O. D. Sherby, J. Wadsworth, Progress in Materials Science 33 (1989) 169-221.

[6] J. W. Edington, Met Trans A - Physical Metallurgy and Materials Science 13 (1982) 703-715.

[7] N. Furushiro, S. Hori, Scripta Metallurgica 13 (1979) 653-656.

[8] A. E. Geckinli, C. R. Barrett, Journal of Materials Science 11 (1976) 510-521.

[9] M. F. Ashby, R. A. Verrall, Acta Metallurgica 21 (1973) 149-163.

[10] J. W. Edington, K. N. Melton, C. P. Cutler, Progress in Materials Science 21 (1976) 63-170.

[11] A. K. Mukherjee, Annual Review of Materials Science 9 (1979) 191-217.

[12] D. M. R. Taplin, G. L. Dunlop, T. G. Langdon, Annual Review of Materials Science 9 (1979) 151-189.

[13] O. A. Kaibyshev, Superplasticity of Alloys, Intermetallics, and Ceramics, Springer-Verlag, New York, 1992.

[14] J. Pilling, N. Ridley, Superplasticity in Crystalline Solids, IOM, 1989.

[15] M. A. Clark, T. H. Alden, Acta Metallurgica 21 (1973) 1195-1206.

[16] K. Holm, J. D. Embury, G. R. Purdy, Acta Metallurgica 25 (1977) 1191-1200.

[17] M. K. Rabinovich, V. G. Trifonov, Acta Materialia 44 (1996) 2073-2078.

[18] H. C. H. Carpenter, C. F. Elam, Journal of the Institute of Metals 24 (1920) 83-154.

[19] T. Sutoki, Science Reports of the Tohoku Imperial University, Series 1: Mathematics, Physics, Chemistry (1928).

[20] M. Hillert, Acta Metallurgica 13 (1965) 227-&.

[21] J. E. Burke, D. Turnbull, Progress in Metal Physics 3 (1952) 220-292.

[22] P. Feltham, Acta Metallurgica 5 (1957) 97-105.

[23] H. V. Atkinson, Acta Metallurgica 36 (1988) 469-491.

[24] M. P. Anderson, D. J. Srolovitz, G. S. Grest, P. S. Sahni, Acta Metallurgica 32 (1984) 783-791.

[25] D. J. Srolovitz, M. P. Anderson, P. S. Sahni, G. S. Grest, Acta Metallurgica 32 (1984) 793-802.

[26] C. Devadas, I. V. Samarasekera, E. B. Hawbolt, Metallurgical Transactions a-Physical Metallurgy and Materials Science 22 (1991) 335-349.

[27] G. Wensch, W. C. Ellis, C. Zener, T. S. Ke, J. W. Fredrickson, H. Eyring, Transactions of the American Institute of Mining and Metallurgical Engineers 185 (1949) 315-318.

[28] C. H. Caceres, D. S. Wilkinson, Acta Metallurgica 32 (1984) 415-422.

[29] D. J. Sherwood, C. H. Hamilton, Scripta Metallurgica Et Materialia 25 (1991) 2873-2878.

[30] D. S. Wilkinson, C. H. Caceres, Acta Metallurgica 32 (1984) 1335-1345.

[31] F. J. Humphreys, Acta Materialia 45 (1997) 5031-5039.

[32] R. W. Cahn, Haasan, P., Physical Metallurgy, Elsevier Science B.V., Amsterdam, 1996.

[33] F. J. Humphreys, Acta Materialia 45 (1997) 4231-4240.

[34] R. D. Doherty, D. A. Hughes, F. J. Humphreys, J. J. Jonas, D. J. Jensen, M. E. Kassner, W. E. King, T. R. McNelley, H. J. McQueen, A. D. Rollett, Materials Science and Engineering a-Structural Materials Properties Microstructure and Processing 238 (1997) 219-274.

[35] T. Sakai, J. J. Jonas, Acta Metallurgica 32 (1984) 189-209.

[36] R. Sandstrom, R. Lagneborg, Acta Metallurgica 23 (1975) 387-398.

[37] R. Sandstrom, R. Lagneborg, Scripta Metallurgica 9 (1975) 59-65.

[38] B. Derby, Scripta Metallurgica Et Materialia 27 (1992) 1581-1586.

[39] P. Peczak, Acta Metallurgica Et Materialia 43 (1995) 1279-1291.

[40] S. R. Chen, U. F. Kocks, Scripta Metallurgica Et Materialia 27 (1992) 1587-1592.

[41] E. Nembach, G. Neite, Progress in Materials Science 29 (1985) 177-319.

[42] E. J. Payton, Factors Affecting Grain Growth During Processing of Advanced Ni-based Disk Superalloys, in: Ohio State University, 2006.

[43] R. D. Kissinger, Superalloys 1996 (1996).

[44] N. Biery, M. De Graef, T. M. Pollock, Met Trans A - Physical Metallurgy and Materials Science 34A (2003) 2301-2313.

[45] A. Wu, Local Strain Development in High Temperature Rual Intermetallic Alloys, in: Materials Science and Eningeering, vol Ph.D, University of Michigan, Ann Arbor, 2006.

[46] K. S. Chan, Journal of Engineering Materials and Technology-Transactions of the Asme 123 (2001) 281-286.

[47] K. S. Chan, L. Perocchi, G. R. Leverant, Metallurgical and Materials Transactions a-Physical Metallurgy and Materials Science 31 (2000) 3029-3040.

[48] P. C. McKeighan, A. E. Nicholls, L. C. Perocchi, R. C. McClung, Sensing crack nucleation and growth in hard alpha defects embedded in Ti-6Al-4V alloy, in: G. F. Lucas, P. C. McKeighan, J. S. Ransom (Eds.), Nontraditional Methods of Sensing Stress, Strain, and Damage in Materials and Structures: Second Volume, vol 1323, 2001, pp. 15-35.

[49] T. H. Alden, Acta Metallurgica 10 (1962) 653-&.

[50] I. F. Collins, S. A. Meguid, Journal of Applied Mechanics-Transactions of the Asme 44 (1977) 271-278.

[51] S. R. Reid, T. Y. Reddy, International Journal of Solids and Structures 14 (1978) 213-225.

[52] Rodrigue.Da, Journal of Applied Mechanics 35 (1968) 173-&.

[53] E. A. Davis, Journal of Applied Physics 8 (1937) 213-217.

[54] A. Nadai, Journal of Applied Physics 8 (1937) 205-213.

[55] W. R. Kerr, Journal of Materials Science 15 (1980) 3104-3108.

[56] R. C. Gifkins, T. G. Langdon, Materials Science and Engineering 36 (1978) 27-33.

[57] S. Consulting, The experimental set up for EBSD, in: Oxford Instruments, 2005.

[58] A. J. Schwartz, Kumar, M., Adams, B.L., Electron Backscatter Diffraction and Future Directions, Kluwer Academic/Plenum Publishers, 2000.

[59] M. Kamaya, A. J. Wilkinson, J. M. Titchmarsh, Nuclear Engineering and Design 235 (2005) 713-725.

[60] M. Kamaya, A. J. Wilkinson, J. M. Titchmarsh, Acta Materialia 54 (2006) 539-548.

[61] D. D. P. F. Wei, R88DT Gamma Prime Equilibrium Volume Fraction, in: 2009.

[62] F. J. H. Humphreys, M., Recrystallization and Related Annealing Phenomena, Elsevier Ltd, Oxford, UK, 2004.

[63] G. Wang, D. S. Xu, N. Ma, N. Zhou, E. J. Payton, R. Yang, M. J. Mills, Y. Wang, Acta Materialia 57 (2009) 316-325.

[64] K. Song, M. Aindow, Materials Science and Engineering a-Structural Materials Properties Microstructure and Processing 479 (2008) 365-372.

[65] E. J. Payton, Characterization of Post-Deformation Microstructures for Incorporation into Phase Field Model of Grain Growth in Ni-based Superalloy, in: TMS 2007, Orlando, FL, 2007.

[66] B. E. Barry, A. F. Brown, Acta Metallurgica 12 (1964) 209-&.

[67] A. O. Alniak, F. Bedir, Materials Science and Engineering B-Solid State Materials for Advanced Technology 130 (2006) 254-263.

[68] K. E. E. D.A. Porter, Phase Transformations in Metals and Alloys, CRC Press, 1992.

[69] F. P. E. Dunne, M. M. Nanneh, M. Zhou, Philosophical Magazine A-Physics of Condensed Matter Structure Defects and Mechanical Properties 75 (1997) 587-610.

[70] D. Y. Cai, L. Y. Xiong, W. C. Liu, G. D. Sun, M. Yao, Materials & Design 30 (2009) 921-925.

[71] A. K. Koul, J. P. A. Immarigeon, Acta Metallurgica 35 (1987) 1791-1805.

[72] E. I. Poliak, J. J. Jonas, Acta Materialia 44 (1996) 127-136.

[73] R. E. Reed-Hill, Physical Metallurgy Principles, Litton Educational Publishing, 1973.

[74] L. J. Carroll, Q. Feng, T. M. Pollock, Met Trans A - Physical Metallurgy and Materials Science 39A (2008) 1290-1307.

[75] T. M. Pollock, A. S. Argon, Acta Metallurgica Et Materialia 40 (1992) 1-30.

[76] H. Mecking, U. F. Kocks, Acta Metallurgica 29 (1981) 1865-1875.

[77] R. W. Kozar, A. Suzuki, W. W. Milligan, J. J. Schirra, M. F. Savage, T. M. Pollock, Met Trans A - Physical Metallurgy and Materials Science 40A (2009) 1588-1603.

[78] E. A. Bonifaz, N. L. Richards, International Journal of Plasticity 24 (2008) 289-301.

[79] Y. Estrin, H. Mecking, Acta Metallurgica 32 (1984) 57-70.